DYNAMIC DECOUPLING AND NOISE ANALYSIS FOR SIMULTANEOUS TRANSMISSION AND RECEPTION IMAGING

A THESIS SUBMITTED TO

THE GRADUATE SCHOOL OF ENGINEERING AND SCIENCE

OF BILKENT UNIVERSITY

IN PARTIAL FULFILLMENT OF THE REQUIREMENTS FOR

THE DEGREE OF

MASTER OF SCIENCE

IN

ELECTRICAL AND ELECTRONICS ENGINEERING

By

Bilal Taşdelen

August 2020

Dynamic Decoupling and Noise Analysis for Simultaneous Transmission and Reception Imaging
By Bilal Taşdelen
August 2020

We certify that we have read this thesis and that in our opinion it is fully adequate, in scope and in quality, as a thesis for the degree of Master of Science.

Ergin Atalar(Advisor)

Emine Ülkü Sarıtaş Çukur

Nevzat Güneri Gençer

Approved for the Graduate School of Engineering and Science:

Ezhan Karaşan
Director of the Graduate School

ABSTRACT

DYNAMIC DECOUPLING AND NOISE ANALYSIS FOR SIMULTANEOUS TRANSMISSION AND RECEPTION IMAGING

Bilal Taşdelen
M.S. in Electrical and Electronics Engineering
Advisor: Ergin Atalar
August 2020

In simultaneous transmission and reception (STAR) MRI, along with the coupling of the excitation pulse to the received signal, noise, and undesired distortions (spurs) coming from the transmit chain also leak into the acquired signal and degrade image quality. The properties of this coupled noise and its relationship with the transmit amplifier gain, transmit chain noise density, isolation performance, and imaging bandwidth are analyzed. The importance of achieving high isolation and careful selection of the corresponding parameters are demonstrated. A cancellation algorithm, together with a vector modulator, is used for transmit-receive isolation. With higher isolation, coupled transmit noise can be reduced to the point that the dominant noise source becomes acquisition noise, as in the case for pulsed MRI. Amplifiers with different gain and noise properties are used in the experiments to verify the derived noise-transmit parameter relation. With the proposed technique, more than 80 dB isolation in the analog domain is achieved. The leakage noise and the spurs coupled from the transmit chain are reduced. It is shown that the transmit gain plays the most critical role in determining sufficient isolation, whereas the amplifier noise figure does not contribute as much.

Additionally, the active cancellation technique mentioned above is adapted to Magnetic Particle Imaging (MPI) for active cancellation of the direct-feedthrough. A significant increase of up to 40 dB in detection sensitivity at the fundamental harmonic on an in-house Arbitrary Waveform Relaxometer (AWR) is demonstrated.

Keywords: Magnetic reconance imaging (MRI), STAR, transmit and receive noise, active cancellation, magnetic particle imaging (MPI).

ÖZET

EŞ ZAMANLI ALICI VERİCİ YAPILI GÖRÜNTÜLEME İÇİN DİNAMİK AYRIŞTIRMA VE GÜRÜLTÜ ANALİZİ

Bilal Taşdelen
Elektrik ve Elektronik Mühendisliği, Yüksek Lisans
Tez Danışmanı: Ergin Atalar
Ağustos 2020

Eş zamanlı alıcı-vericili MR görüntülemede, uyarı darbesinin alınan sinyale bulaşmasının yanı sıra, verici yapısından gürültü ve istenmeyen bozulmalar da alınan sinyale sızar ve görüntü kalitesini düşürür. Burada, bu bulaşmış gürültünün ve verici yükselteci kazancının özellikleri, verici yapısı gürültü yoğunluğu, ayrıştırma performansı ve görüntüleme bant genişliği incelenmiştir. Yüksek ayrıştırma sağlamanın ve alakalı parametrelerin özenle seçilmesinin önemi gösterilmiştir. Alıcı-verici ayrıştırması, bir vektör modülatörü ile birlikte bir ayrıştırma algoritması kullanılarak sağlanmıştır. Yüksek ayrıştırma ile birlikte darbeli MRG'de olduğu gibi, bulaşan verici gürültüsü, baskın gürültü kaynağı imge elde etme gürültü seviyesi baskın olana kadar düşürülmüştür. Türetilmiş gürültü-verici parametre ilişkisini doğrulamak için farklı kazanç ve gürültü özelliklerine sahip yükselteçlerin kullanıldığı deneyler yapılmıştır. Önerilen teknik ile birlikte, analog alanda 80 dB'den fazla ayrıştırma sağlanmıştır. Verici yapısından sızan gürültü ve bozulmalar azaltılmıştır. Gereken ayrıştırma miktarının sağlanmasında en önemli rolu oynayanın verici kazancı olduğu, yükselteç gürültüsünün fazla katkı sağlamadığı gösterilmiştir.

Ek olarak, yukarda bahsedilen aktif ayrıştırma tekniği, Manyetik Parçacık Görüntülemede (MPG) direk-beslemenin aktif olarak silinmesi için uyarlanmıştır. Temel frekansta tespit yeteneğinin önemli bir oranda (40 dB'ye kadar) arttığı ev yapımı bir rastgele dalga biçimi relaksometresinde gösterilmiştir.

Anahtar sözcükler: Manyetik Rezonans Görüntüleme (MRG), STAR, alıcı ve verici gürültüsü, aktif ayrıştırma, manyetik parçacık görüntüleme (MPG).

Acknowledgement

First of all, I would like to thank my supervisor, Prof. Ergin Atalar, for his endless support throughout my undergraduate years and master's thesis. During my undergraduate internship in UMRAM, his enthusiasm and encouragements made me pursue an academic path in medical imaging, in which I found my passion. Because of his encouragement, I was able to carry on even the hardest of the tasks during my academic life. He was not solely an advisor for me on my thesis, but he was a guide for me and shed light on my further academic pursuits.

I would like to thank Assoc. Prof. Emine Ülkü Sarıtaş, for her guidance and help on my thesis. Thanks to her, I was able to extend my thesis further. It was a delight to work with her. I was able to learn many things apart from my main subject, which I believed help me to think more out of the box.

Also, I would like to thank both Assoc. Prof. Emine Ülkü Sarıtaş and Prof. Nevzat Güneri Gençer for being in my thesis committee. I believe, thanks to their feedback, this work is much more complete and valuable.

I also want to thank my friends. Thanks to my roommates, Muhammed, Burak, Ömer and Abdulsamet, I had lots of fun and joy during my years in Bilkent. Thanks to my coauthors Alireza and Uğur. We had very fruitful discussions and many productive and fun hours together. This work is more complete thanks to them. Thanks to Cemre, Süheyl, and Koray, their guidance was fundamental especially more in my first years. Thanks to the rest of my UMRAM family, Salman, Alper, Mert, Muzaffer, Mustafa, Rahmi, Emin, Toygan, Özgür, Ehsan, Reza, Said, and many others that I did not write here, but all of them touched my heart. I also want to thank my classmates and friends from the department, Mahmut, Erdem, İbrahim, Kübra, and Dilan. Thanks to my friends in "Samedu" and "CS:G0". Thank you for cheering me up, putting up with me and supporting me all these years. I feel like I have grown up together with all of you.

I would like to thank my fiancee, soon to be wife Ecrin Yağız. She was always

there for me during most of my years in Bilkent. I was lucky to benefit the most from her admirable smarts and moral support. She is my best friend, most valuable coworker, and partner in crime. She was my joy throughout all these years. I am looking forward to many years to come. I believe we are "synergistic".

I wish to thank my family, for everything I have in my life. Without their moral and material support, I could not achieve anything in this life. They were always there for me when I need them. In my every decision, I knew I could count on them. It is impossible for me to pay them back. I hold my dear sister, İkbal as a blessing. I know that she will well surpass what I have achieved, she is a gift to our family. I will always pray for her well-being and success.

Contents

1 Introduction **1**

2 Background Information **4**

2.1 STAR 4

2.2 MRI Signal Equation 6

2.3 Continuous SWIFT 9

2.3.1 Gridding 10

2.4 MPI Principles 11

3 Analysis and Mitigation of Noise in Simultaneous Transmission and Reception in MRI **13**

3.1 Introduction 13

3.2 Theory 16

3.2.1 Signal Description in STAR 16

3.2.2 Noise and Spurs 16

3.2.3 Signal Equation 18

3.3 Methods 20

3.3.1 Hardware 20

3.3.2 Imaging Experiments 24

3.3.3 Image Reconstruction 26

3.3.4 Deconvolution 27

3.3.5 Noise Experiments 29

3.4 Results 31

3.5 Discussion 33

4 A Look-up Table Based Algorithm for Dynamic Cancellation in Simultaneous Transmission and Reception 37

4.1 Introduction 37

4.2 Theory 38

4.2.1 Constellation Construction 40

4.2.2 Cancellation Loop 42

4.3 Methods 44

4.4 Results 44

4.5 Discussion 45

5 Vector Modulator Based Active Compensation of Direct

Feedthrough in Magnetic Particle Imaging **49**

5.1 Introduction 49

5.2 Material and Methods 50

5.2.1 Active Compensation Circuit 51

5.2.2 Experiment Setup 53

5.3 Results 54

5.4 Discussion 56

6 Conclusion **58**

A Calculation of the Component Values **67**

A.1 Phase Shifters 67

A.2 Wilkinson Divider 68

List of Figures

2.1 **(A)** Full-duplex transmission and reception, or STAR example. **(B)** Half-duplex, time multiplexed transmission and reception. With this type of transmit and receive, there is a dead time in between the beginning of transmission and the beginning of the reception, denotes as Δt. STAR eliminates this dead time. **(C)** Simplified signal paths during STAR. In half-duplex communication or imaging, only the paths denoted by the blue arrows exist. In STAR, an additional and undesired path exists between transmit and receive antennas, denoted by the red arrow. 5

2.2 **(A)** Diagram of the pulse sequence for one TR. Gradients in x, y and z directions are swept in order to scan the intended trajectory. **(B)** Radial trajectory as scanned by the pulse sequence diagram in (A). Trajectory is scanned in k_r direction for every line. For each line, k_r is rotated by $\Delta\phi$ in the direction of ϕ in order to cover the whole k-space. 9

2.3 Illustration of the magnetization of SPIOs under sinusoidal drive field. This type of magnetization only occurs in the FFP, meanwhile the other points in the space are completely saturated, and does not react to drive field. Signal induced on the receive coil and its frequency spectrum due to such magnetization is also illustrated. Contamination of drive field at the fundamental frequency is shown as the red bar on the spectrum, and typically dominates the particle signal amplitude at the fundamental frequency. 12

3.1 Schematic description of the STAR system and the MRI scanner. **(A)** Overall system diagram. Measurements are read from the scanner after digitization via real-time data transfer functionality. **(B)** Implementation of the Wilkinson Power Divider/Combiner as proposed in Okada et al. [1]. **(C)** Implementation of the fixed phase shifters. 21

3.2 **(A)** Schematic of the Equal Wilkinson Power Divider. If unequal power division is desired, additional matching circuitry is required after the division ports. **(B)** Schematic of the 4-way divider and fixed phase shifters. Fixed phase shifters are only implemented in the division part. At the combiner part, necessary places are bypassed via shorting. **(C)** PCB layouts of the circuits. 1- Connector module that distributes power and control signals to the attenuators. 2- Layout of the circuit at (B). 3- Layout of the Equal Wilkinson Divider in (A). 4- Layout of the attenuators. **(D)** Image of the vector modulator. Parts are annotated according to the numbers in (C). 22

3.3 **(A)** 3D Model of the birdcage coil. The outer cylinder is the shield, and it is shifted to reveal the coil frame. The coil frame can be seen as the inner cylinder, and the copper parts and ports are visible. **(B)** S-parameter measurements of the constructed coil. 40 dB isolation is achieved at the center frequency. Isolation is more than 30 dB in a 1 MHz bandwidth around the center frequency. . 23

3.4 Photographs of the experiment setup. **(A)** Overall experiment setup. **(B)** Imaging phantoms and their placements in the coil. **(C)** Vector modulator. Circuit is connected to the coil, the power low-noise amplifier (PLNA) and the LNA via Wilkinson Power Dividers/Combiners. **(D)** Raspberry Pi 3B+ communicates and powers the vector modulator. 25

3.5 Image before **(A)** and after **(B)** the bullseye filtering. In (A), more ring-like artifacts are visible compared to (B). No distortion is observed on the image due to the filtering. It can be seen that, the bullseye filtering does not reduce the artifacts caused by other sources, such as susceptibility. 29

3.6 Schematics of the noise experiments. Experiments 3, 4 and 5 are repeated for power low-noise amplifier (PLNA), cascaded power low-noise amplifier ($PLNA^2$), and Analogic transmit power amplifier (ATPA). An attenuator of known value after the transmit chain is used when necessary to protect receive chain from saturation and damage. 30

3.7 Gains and output referred noise powers are annotated on the system schematic. Gains and noise spectral density of PLNA, $PLNA^2$, and LNA, as well as gain of the coil and noise spectral density of the vector modulator is measured with a network analyzer and noise figure meter, and also verified with scanner measurements. . 31

3.8 Noise PSD for three noise experiments (experiments 3, 4 and 5) and amplifiers PLNA, PLNA^2, and ATPA. Red dashed line marks the minimum achievable noise level. **(A)** Low frequency (5.6 kHz) harmonics that can be seen in PLNA and PLNA^2 are coupling from the power supply of custom amplifiers. At ATPA, phase noise can be observed at ATPA as the spread around the center frequency. **(B)** After passive isolation (40 dB), it can be observed that both noise and spur is reduced significantly. Since thermal noise is also reduced, some peaks that were not visible became visible. **(C)** After active isolation with the isolation threshold 80 dB, most peaks are cleared out. 35

3.9 **(A) - (C)** are reference 2D GRE images with FOV 250x250 mm, 256x230 matrix size and 81.92 kHz bandwidth. cSWIFT images **(D)-(F)** acquired with 2.56 kHz bandwidth and **(G)-(I)** acquired with 6.4 kHz bandwidth. 36

4.1 The decoupling algorithm. **(A)** Flow chart of the compensation loop. $\hat{c}$, $\hat{l}$ and $\hat{s}_{\text{comp}}$ can be considered as estimated $X(f)$, $L(f)$ and $Y(f, \boldsymbol{x})$ at the center frequency respectively. **(B)** Model assumed on the vector modulator. In other terms, the output s_{comp} is the weighted combination of the input $c \cdot s_{\text{Tx}}$ by the complex weight a_i of each line. **(C)** A representative visualization of the constellation. Each point represents the value of the transfer function at the center frequency for a given $\boldsymbol{x}$ vector. A subsection divided according to the phase and the amplitude can be seen as the yellow part. 38

4.2 **(A)** Isolation performance with the coil measurement given in Fig. 3.3-B. -80 dB bandwidth is around 10 kHz. Digital inputs of the attenuators are optimized to minimize $|S_{21}|$ of the system. **(B)** Vector modulator S-parameters when the attenuator inputs are set as in A. The amplitude variation is around 0.3 dB and the angle variation is around 6°in 1 MHz bandwidth. 45

4.3 Isolation performance graphics. **(A)** Network analyzer experiment in a stable environment (e.g. load is static, no vibration around coil etc.). **(B)** Same experiment with a), but this time hand movement is present in the vicinity of the coil. **(C)** Decoupling performance in MRI scanner. Note that, due to vector modular output being higher than the leak signal, initial value for isolation does not represent passive cancellation. **(D)** G_{isol} ($|S_{21}|$) of the actively isolated system and its -60 dB and -80 dB bandwidth values. 46

5.1 **(A)** Schematic of the in-house AWR. **(B)** Schematic of the system and compensation circuit, which acts as a vector modulator. . . . 51

5.2 **(A)** The fabricated manually controlled vector modulator. **(B)** PCB layout of the manually controlled vector modulator. **(C)** 3D model of the manually controlled vector modulator. **(D)** The fabricated digitally controlled vector modulator. **(E)** PCB layout of the manually controlled vector modulator **(F)** 3D model of the manually controlled vector modulator. 52

5.3 **(A)** Schematic of the LTSpice simulation of AWR setup and the vector modulator. **(B)** Frequency response of the schematic simulated between 1 kHz to 1MHz. $V(ft)$ is the direct-feedthrough voltage measured at the receive coil. $V(comp)$ is the compensation signal measured at the output of the vector modulator. The cursor marks the value at 10.8 kHz. **(C)** Frequency response of the compensated received signal. $V(Comp, FT)$ is the difference between feedthrough and the compensation signal ($V(ft) - V(comp)$). The cursor marks the value at 10.8 kHz. 54

5.4 Signal at the fundamental harmonic and the third harmonic, with and without active compensation for four samples with different dilution factors. $f_0 = 10.8$ kHz. 55

5.5 Line scan of a phantom without **(A)** and with **(B)** active compensation. 56

A.1 **(A)** High-pass tee phase shifter. **(B)** Two high-pass tee phase shifter in series for doubling phase shift. **(C)** High-pass pi phase shifter. 67

A.2 **(A)** Schematic of the Wilkinson Power divider. If an unequal division ratio is desired, additional matching circuitry is required after the Port 2 and Port 3. **(B)** Even-mode analysis of the circuit. **(C)** Odd-mode analysis of the circuit. **(D)** Matching circuits for the Port 2 (top) which satisfies $R_2 < Z_0$ and for the Port 3 (bottom) which satisfies $R_3 > Z_0$ by convention. 69

List of Tables

3.1 Noise spectral density for the Larmor frequency for each experiment. Noise measurements are acquired when RF voltage is set to 0 Volts. For verification, these measurements are compared to the background noise level with the experiment when RF power is present. 32

Chapter 1

Introduction

Magnetic resonance imaging (MRI) is an essential imaging modality, and it is commonly used for both clinical and scientific purposes. Due to its importance in clinical applications, it has been the center of attention for many researchers throughout its history. Its potential comes from the fact that it is a non-invasive and safe diagnostic tool. It is exceptionally flexible since it allows the user to image various contrasts, acquire quantitative maps. Furthermore, it is possible to extract clinically valuable information with MRI, such as temperature, conductivity and stiffness maps.

This thesis tries to extend the capabilities of MRI via proposing a method to enable simultaneous transmission and reception (STAR) in MRI, analyzing the noise properties during STAR imaging and mitigating the excess noise caused by the coupling between the transmit and the receive coil. In this thesis, it is demonstrated that STAR imaging in MRI can be achieved in a fast and dynamic way, which increases the stability of the system in the presence of load variations to the coil by controlling a vector modulator with the proposed algorithm. Additionally, it is shown that noise coupled from the transmit path to the receive path can be reduced with this setup. The system parameters and requirements are also investigated regarding the coupled noise in order to layout the system parameters, decoupling performance and image SNR relation, and provide a framework

for future research in this area.

In this thesis, some of the work regarding STAR imaging is also transferred to magnetic particle imaging (MPI). MPI is a rapidly developing imaging technique that images the spatial distribution of superparamagnetic iron oxide (SPIO) nanoparticles [2, 3, 4]. It has excellent potential for many clinical applications such as angiography [5], stem cell imaging [6], multi-color imaging [7], viscosity mapping [8, 9], and functional imaging [10]. It is demonstrated that using similar techniques that have been used in STAR MRI to isolate the transmit and receive coil, self-interference (referred to as direct-feedthrough in MPI) can also be removed. As a result, sensitivity can be increased and information loss due to direct-feedthrough can be avoided.

Outline of the Thesis

Chapter 4 introduces a novel algorithm to achieve fast and dynamic active decoupling. The principles and the construction of the hardware and experiment setup necessary to demonstrate the algorithm is given in this chapter as well. It is shown that, using the proposed algorithm together with a digitally controlled vector modulator, high isolation can be achieved in a short time, allowing STAR imaging even in the presence of load variations. Future modifications and the extensions of the algorithm is discussed that can possibly enable real-time tracking and cancellation of the leak signal. The proposed algorithm is not necessarily restricted to MRI and MPI, however implementation and experimentation is mainly done on MRI.

Chapter 3 analyzes the noise and spurs coupling to the image during STAR imaging analytically and experimentally using the proposed STAR system in the Chapter 4. Parameters such as transmit gain, noise, imaging bandwidth, and isolation level are investigated, and their relationships with each other are derived and verified with experiments. It is claimed that, these parameters can be used while designing a STAR enabled system to determine necessary isolation level

and transmit chain gain and noise. Images acquired with the STAR technique is also shown and evaluated.

The contribution of the author of this thesis for the works in Chapter 4 and Chapter 3 are summarized here. Birdcage coil design and simulations are done by coauthor Alireza Sadeghi-Tarakameh. Uğur Yılmaz developed the real-time feedback communication software on MRI scanner and advised on the pulse sequence development, and is a coauthor. Rest of the work that can be summarized as hardware development and fabrication, coil fabrication, pulse sequence development and implementation, algorithm development and implementation, image reconstruction development and implementation, analytical derivation and analysis, experimental derivation and analysis, is done by the author of this thesis.

Chapter 3 proposes a similar structure that actively cancels out direct feedthrough by a manually tuned vector modulator for MPI. The benefits of removing the direct feedthrough in the analog domain are shown by the experiments using an Arbitrary Waveform Relaxometer (AWR), and the possibility of increasing the SPIO detection sensitivity is demonstrated. Merits of utilizing active cancellation in analog domain and using a correlated signal and noise source is demonstrated and discussed.

The contribution of the author of this thesis for this work is summarized here. Experiment design and acquisition on AWR is done by coauthor Ecrin Yağız. MPI experiments are done by coauthor Mustafa Ütkür. Gradiometer design is done by a coauthor Ahmet R. Çağıl. AWR design is done by a coauthor Can Barış Top. Rest of the work that can be summarized as design, simulation, and fabrication of the vector modulator, and experimentation related to active compensation is done by the author of this thesis.

Finally, in Chapter 6, all the findings in this thesis are summarized.

Chapter 2

Background Information

In this section, some background information related to the topics of this thesis is covered. This section can be skipped if the reader is not interested in MRI signal equation, radial trajectory and continuous SWIFT pulse sequence or basic MPI principles. Following chapters are self-contained and further explore aforementioned topics.

2.1 STAR

In time-multiplexed communication, transmission and reception occur in distinct time instances, whereas in simultaneous transmission and reception, or STAR, in short, these events happen concurrently. Pulsed MRI, in this aspect, resembles the time-multiplexed, half-duplex communication. In conventional pulsed MRI, there is a dead time between the start of the excitation and the start of the reception. STAR, on the other hand, being full-duplex, eliminates this dead time. This is illustrated in the Fig. 2.1.

Compared to the pulsed MRI, STAR imaging has some advantages. It can be faster since the dead time is eliminated. For communication, it can be thought as doubling the bandwidth. There is less signal decay due to relaxation in MRI,

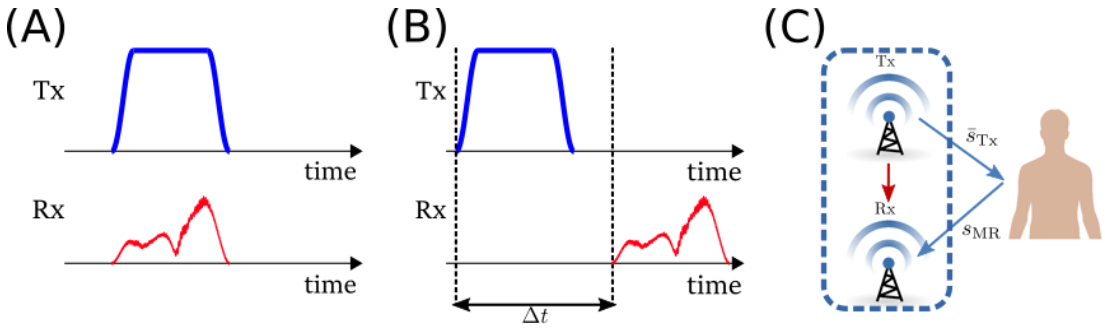

Figure 2.1: **(A)** Full-duplex transmission and reception, or STAR example. **(B)** Half-duplex, time multiplexed transmission and reception. With this type of transmit and receive, there is a dead time in between the beginning of transmission and the beginning of the reception, denotes as Δt. STAR eliminates this dead time. **(C)** Simplified signal paths during STAR. In half-duplex communication or imaging, only the paths denoted by the blue arrows exist. In STAR, an additional and undesired path exists between transmit and receive antennas, denoted by the red arrow.

signal can be recorded before it decays. Due to this, it is possible to image fast decaying tissues that have short T_2 with this method such as bones and cartilages. Also, less RF power is required to achieve a similar SNR [12].

However, together with the advantages, there are also challenges, such as the time-varying RF self-interference between transmit and receive antennas is unavoidable when transmission and reception occur simultaneously. Together with the self-interference, transmit noise also couples to the received signal and cripples the SNR. This coupling can be modeled as the following equation:

$$s_{\mathrm{Rx}}(t) = s_{\mathrm{MR}}(t) + A(t) \cdot e^{i\phi(t)} \cdot \bar{s}_{\mathrm{Tx}}(t) \tag{2.1}$$

Here $s_{\mathrm{Rx}}(t)$ is the received signal from the receive antenna. $s_{\mathrm{MR}}(t)$ is the desired signal, which is the MR signal in this case. $\bar{s}_{\mathrm{Tx}}(t)$ is the transmitted waveform. $A(t)$ and $\phi(t)$ is the time varying coupling coefficient amplitude and phase respectively.

This self-interference is usually reduced in various ways. Passive isolation methods such as antenna isolation are usually employed to minimize the coupling

coefficient $A(t)$. Passive isolation methods are convenient since they do not require any effort to work after the implementation. However, isolation provided by these methods is usually not sufficient, and they fail to adapt to the time-varying nature of the self-interference.

Residual interference can be digitally removed after the sampling by estimating the $A(t)$ and $\phi(t)$ and utilizing the knowledge of the transmitted signal. This method is quite convenient as well since it does not require any modification to the hardware. However, with this method, even if the original signal envelope can be successfully removed, unknown distortions and coupled transmit noise may not be effectively reduced, which will cripple the SNR.

With the active cancellation, the aforementioned shortcomings can be solved. Active cancellation methods aim to adapt the time varying nature of the leak signal by monitoring and minimizing it. However, they require additional hardware to monitor the leak or control the active cancellation hardware. Furthermore, these techniques generally spend additional RF power, which might be precious for some cases. Hence, usually active cancellation methods are applied in conjunction with the passive isolation methods to reduce power requirements.

2.2 MRI Signal Equation

The behavior of the magnetization vector $\boldsymbol{M}$ under the applied magnetic fields $\boldsymbol{B}$ can be expressed by the Bloch equation as following:

$$\frac{d\boldsymbol{M}}{dt} = \boldsymbol{M} \times \gamma \boldsymbol{B} - \frac{M_x \boldsymbol{i} + M_y \boldsymbol{j}}{T_2} - \frac{(M_z - M_0)\boldsymbol{k}}{T_1} \tag{2.2}$$

Here, M_0 is the equilibrium magnetization under the static magnetic field B_0. $\boldsymbol{i}$, $\boldsymbol{j}$ and $\boldsymbol{k}$ are unit vectors in the x, y and z directions respectively. T_1 is the longitudinal relaxation and T_2 is the transverse relaxation [11].

To make the Bloch equations easier to analyze, usually a rotating frame transformation is defined. Relaxations T_1 and T_2 in the Eq. (2.2) will be ignored. Frame of reference to a rotating reference about z with a frequency ω of the excitation field $B_1(t)$ will be transformed. Then let:

$$M_{rot} = \begin{bmatrix} M_{x'} \\ M_{y'} \\ M_z \end{bmatrix}, B_{rot} = \begin{bmatrix} B_{x'} \\ B_{y'} \\ B_z \end{bmatrix} \tag{2.3}$$

so that laboratory frame and rotating frame components are related by $M = R_z(\omega t)M_{rot}$ and $B = R_z(\omega t)B_{rot}$.

Let's define complex representation of the transverse magnetization in rotating frame as:

$$M_r(t) = M_{x'}(t) + iM_{y'}(t) \tag{2.4}$$

Hence, lab and rotating frame are related by $M(t) = M_r(t)e^{-i\omega t}$.

Finally, let's choose rotating unit vectors $\boldsymbol{i'}$ and $\boldsymbol{j'}$ so that:

$$\begin{aligned} \boldsymbol{i'} &= \boldsymbol{i}\cos(\omega t) - \boldsymbol{j}\sin(\omega t) \\ \boldsymbol{j'} &= \boldsymbol{i}\sin(\omega t) + \boldsymbol{j}\cos(\omega t) \end{aligned} \tag{2.5}$$

Then,

$$M_x(t)\boldsymbol{i} + M_y(t)\boldsymbol{j} = M_{x'}(t)\boldsymbol{i'} + M_{y'}(t)\boldsymbol{j'} \tag{2.6}$$

With this transformation, Bloch equation becomes:

$$\frac{dM_{rot}}{dt} = M_{rot} \times \gamma B_{eff} \tag{2.7}$$

where

$$B_{eff} = B_{rot} + \frac{-\omega}{\gamma}\begin{bmatrix} 0 & 0 & 1 \end{bmatrix} \tag{2.8}$$

Let the applied gradient fields be $G(x, y, z) = G_x x + G_y y + G_z z$ in three spatial dimensions with the amplitudes G_x, G_y and G_z in the x, y and z direction respectively. Define $G(r) = G_r r = G(x, y, z)$ such that $G_r = \sqrt{G_x^2 + G_y^2 + G_z^2}$ and $r = \frac{G_x x + G_y y + G_z z}{\sqrt{G_x^2 + G_y^2 + G_z^2}}$, hence r corresponds to the spatial direction that is defined by the vector $[G_x, G_y, G_z]$. Ignoring the relaxations, in rotating coordinate system and under the small tip-angle approximation, under gradient fields $G(r)$ and RF field $B_1(t)$, Bloch equation can be simplified as:

$$\begin{bmatrix} \frac{dM_{x'}}{dt} \\ \frac{dM_{y'}}{dt} \\ \frac{dM_z}{dt} \end{bmatrix} = \begin{bmatrix} 0 & \omega(r) & 0 \\ \omega(r) & 0 & \omega_1(t) \\ 0 & 0 & 0 \end{bmatrix} \cdot \begin{bmatrix} M_{x'} \\ M_{y'} \\ M_0 \end{bmatrix} \tag{2.9}$$

where $\omega_1(t) = \gamma B_1(t)$ and $\omega(r) = \gamma G(r)$. Equation for the transverse component is:

$$\frac{dM_r}{dt} = -i\omega(r)M_r + i\omega_1(t)M_0 \tag{2.10}$$

Solution to this first order differential equation is:

$$M_r(t, r) = iM_0(r)e^{-i\omega(r)t} \int_0^t e^{i\omega(r)s}\omega_1(s)ds \tag{2.11}$$

Here, $M_0(r)$ corresponds to a projection of the equilibrium magnetization along r.

Signal $s(t)$ generated from the transverse magnetization $M_r(t, r)$ is the integral of the magnetization along r:

$$s(t) = \int_{-\infty}^{\infty} M_r(t, r)dr \tag{2.12}$$

Note that this assumes a perfect B_0 without field inhomogeneity. In the case that inhomogeneity is taken into account, $\omega(r)$ can be written as $\omega(r) = \gamma G(r) + B_e$ where B_e is the effective magnetic field at rotating frame.

2.3 Continuous SWIFT

The pulse sequence and resulting k-space trajectory that is used in this work can be seen in Fig. 2.2. This pulse sequence is also called continuous SWIFT (cSWIFT) and detailed in Idiyatullin et. al. [12].

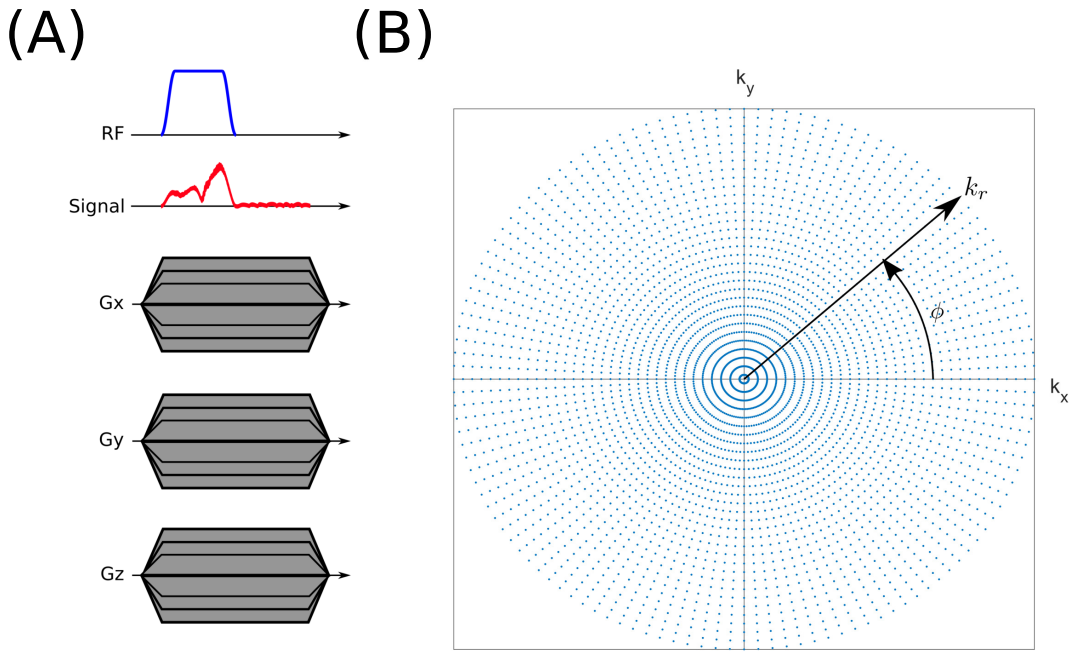

Figure 2.2: **(A)** Diagram of the pulse sequence for one TR. Gradients in x, y and z directions are swept in order to scan the intended trajectory. **(B)** Radial trajectory as scanned by the pulse sequence diagram in (A). Trajectory is scanned in k_r direction for every line. For each line, k_r is rotated by $\Delta\phi$ in the direction of ϕ in order to cover the whole k-space.

Images acquired by the pulse sequence given in Fig. 2.2 provides 2D projections of the 3D volume. This is because, in STAR MRI, there is no slice or slab selection. Thus the signal comes from the whole volume where the coil sensitivity is non-zero. 3D k-space is covered by rotating the 2D k-space trajectory in the other direction, acquiring 2D projections from different angles.

Radial field-of-view (FOV) with this pulse sequence can be calculated as:

$$FOV = \frac{BW_{\mathrm{PP}} \cdot N}{\gamma\!\!\!^{-} G_r} \tag{2.13}$$

where FOV is the radial field of view, N is the number of samples acquired per readout, BW_{PP} is the bandwidth per pixel (imaging bandwidth), and $\gamma\!\!\!^{-} = \frac{\gamma}{2\pi}$, where γ is the gyromagnetic ratio. From there, bandwidth of the RF pulse required to excite the region of interest can be written as:

$$BW = BW_{\mathrm{PP}} \cdot N \tag{2.14}$$

This equation signifies that bandwidth of the RF pulse increases the resolution is increased without reducing the FOV or decrease scan time by increasing the BW_{PP}. Note that, RF pulse is only open for the half duration of the acquisition to reduce the artifacts caused by instability during the reconstruction [13].

Another aspect of the pulse sequence design is the number of required spokes to satisfy the Nyquist criterion. For radial 3D imaging, the number of spokes necessary to meet the Nyquist criterion can be calculated as:

$$N_s = \pi N^2 \tag{2.15}$$

where N_s is the number of spokes required to satisfy the Nyquist criterion [14]. However, unlike the Cartesian case, aliasing in radial trajectory is spread out and noise-like; thus, it does not degrade image quality as much if this criterion is not satisfied. Hence, it is possible to undersample the k-space with radial sampling by sacrificing a little image quality.

2.3.1 Gridding

In the reconstruction of radial pulse sequences in MRI, usually gridding or non-uniform Fourier Transform (NUFFT) is used. In this thesis, gridding is preferred.

By gridding, non-Cartesian k-space samples will be gridded onto Cartesian coordinates, after which Fourier transformation can be used to transform the image to the spatial domain [15]. In this work, the gridding implementation from Hargreaves & Betty [16] is used.

2.4 MPI Principles

In MPI, the nonlinear magnetization of the superparamagnetic iron oxide nanoparticles (SPIO) is exploited for imaging. In a typical MPI scanner, an inhomogenous selection field is used to saturate the nanoparticles that are not positioned in the field-free point (FFP). When a time-varying drive field superimposed to the selection field, SPIOs inside the FFP induce a signal on the receive coil. In contrast, the SPIOs in the other regions do not generate any signal since they are saturated. Nonlinear magnetization of the SPIOs (modeled by Langevin function) generates harmonics of the applied single frequency drive field on top of the fundamental frequency (f_0).

One of the reasonable assumptions in MPI is that, SPIOs align themselves with the applied drive field instantaneously. Hence, drive field application and signal reception occurs simultaneously. Combined with the fact that transmit and receive coils are in close proximity and have positive mutual coupling, the direct-feedthrough is unavoidable. This phenomenon is illustrated in the Fig. 2.3. This direct-feedthrough can be minimized by a passive cancellation approach (usually with a gradiometer design); however, some portion of the coupled drive field remains at the receive side as it is not feasible to eliminate the feedthrough. Also, the amount of residual feedthrough changes over time due to mechanical disturbances in the setup or heating. Hence, the frequency content of the nanoparticle signal coinciding with the drive field frequency is contaminated by the feedthrough. Although this information is partially recovered by some other means, SNR loss and image artifacts may occur. Still, this contamination enforces the usage of single tone drive fields, since inter-modulations of multi-frequency

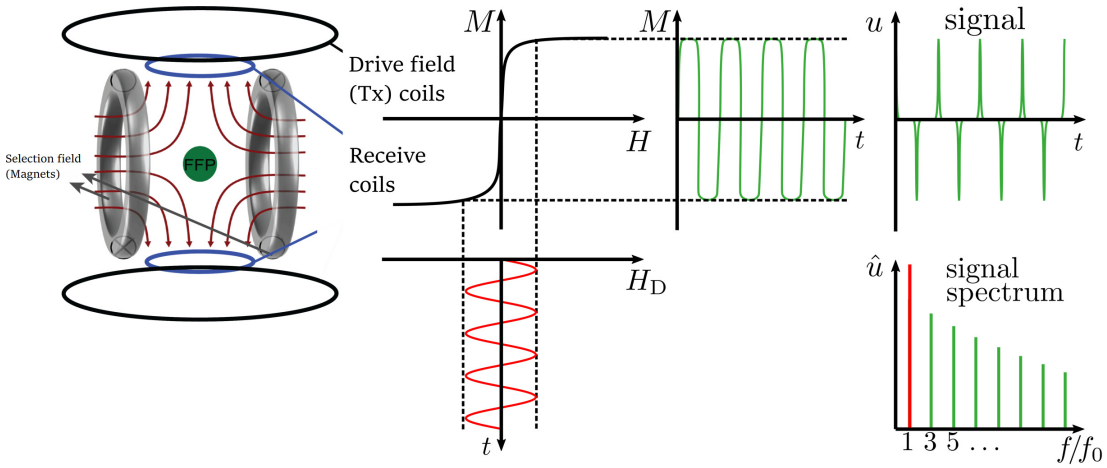

Figure 2.3: Illustration of the magnetization of SPIOs under sinusoidal drive field. This type of magnetization only occurs in the FFP, meanwhile the other points in the space are completely saturated, and does not react to drive field. Signal induced on the receive coil and its frequency spectrum due to such magnetization is also illustrated. Contamination of drive field at the fundamental frequency is shown as the red bar on the spectrum, and typically dominates the particle signal amplitude at the fundamental frequency.

field makes the contamination even worse. Also, the contaminated region accommodates the highest energy. Hence, losing this information reduces the system's detection sensitivity. Moreover, direct-feedthrough decreases the dynamic range, number of usable ADC bits, and together with the drive field, transmit noise also couples.

Chapter 3

Analysis and Mitigation of Noise in Simultaneous Transmission and Reception in MRI

3.1 Introduction

In this work, noise and spurs leaking from the transmit chain to the receive chain and derived the relation between signal-to-noise ratio (SNR) and the transmit chain parameters (e.g., noise performance and gain) are analyzed during simultaneous transmission and reception (STAR) imaging in MRI. This leakage, containing coupled excitation signal, transmit noise and spurious signals, degrades image quality and should be isolated. It has been shown that by using an active cancellation circuit and a control algorithm, it is possible to isolate the noise coming from the leakage, as well as the leakage itself. This work was submitted as an abstract [47] to ISMRM 2020 and presented as a poster presentation. Also this work, together with the work in Chapter 4, submitted as a full paper to the journal Magnetic Resonance in Medicine (MRM) and currently under review.

In pulsed MRI, acquisition and excitation happen in distinct times, exploiting

the slow signal decay of the tissues [18, 19]. This feature simplifies the system greatly by circumventing the issue of self-interference. Due to its convenience and flexibility, pulsed MRI methods are well investigated and widely used over the years. However, pulsed MRI has its disadvantages, such as having a dead time between transmission and reception, which causes signal decay. Signal decay is more prominent with the fast decaying specimens with low T_2 values, including clinically valuable tissues such as bones, ligaments, and teeth [20]. Although there are pulse sequences specifically designed for imaging such tissues (e.g., UTE [21, 22], ZTE [23, 24, 25, 26, 27], SWIFT [28, 29]), they are hardware demanding in terms of fast transmit/receive switching and high slew-rate fast switching gradients. Additionally, most pulse sequences, especially the UTE sequence, often produce high acoustic noise due to fast switching gradients, causing patient discomfort. Due to short RF duration, they deposit high RF power to the body, increasing peak specific absorption rate.

An alternative technique is the STAR imaging, which reduces signal loss since the dead time can be eliminated [30, 31, 32, 33, 12]. This method also has the advantage of acquiring the signal from the tissues with very short T_2 values. There is no need for fast switching gradients in this method implying reduced acoustic noise. Moreover, it is shown that this method requires much less RF power compared to similar nonsimultaneous techniques (e.g., continuous SWIFT vs. SWIFT) [12, 30].

Even though STAR imaging carries the advantages mentioned above, several issues hinder the possibility of clinical usage. Self-interference is the primary consideration that requires handling. Self-interference is time-varying in nature, mostly due to the load and environment variations. It reduces the dynamic range of the receive chain, even to the point of saturation, if unchecked.

There are many active and passive approaches proposed to overcome the self-interference issue. Passive methods such as geometric decoupling [34] and decoupling matrix [35, 36] are already common for the receive-receive isolation and the transmit-transmit isolation, and they can be used for the transmit-receive isolation as well.

For active cancellation, several methods are proposed both in telecommunications [37, 38] and in MRI [31, 39, 30, 32]. Although these methods introduce complexity, are inefficient in terms of power and require specialized hardware, they are necessary to compensate for the time-varying part of the leakage signals.

A challenge regarding the STAR imaging closely related to the self-interference issue, is the injection of the transmit noise and spurs (undesired peaks in the spectrum) into the received signal. Because of this issue, the transmit amplifiers of the scanners are usually replaced with low-noise, low-power amplifiers.

Active cancellation methods can be classified according to the source of compensation signal, i. e. whether the compensation signal is a sample of the original transmit signal, similar to a feedforward path, or created from an independent signal source. This distinction is vital since independent signal sources inject uncorrelated noise and distortions into the reception.

The transmit noise and the spurs that leak to the received signal reduce the SNR and introduce artifacts. Cancellation methods in the analog domain (as opposed to cancellation in post-processing) [30, 32, 17] isolate the transmit noise since it is highly correlated to the noise on the compensation signal. This correlation implies there is a direct relation between SNR and isolation, which is not investigated before. Furthermore, the importance of obtaining high isolation is known for increased dynamic range; however, isolation and SNR relations remain to be analyzed.

In this work, transmit noise and spurs issues, and the trade-off between the transmit chain parameters (gain and noise) that govern the relation between SNR and isolation are investigated. STAR imaging is realized by utilizing a combination of a passive and an active method to verify the findings. For passive isolation, electrical isolation between the ports of a birdcage (BC) coil is exploited. Moreover, a technique recently proposed by the authors of this thesis is used, which enables a fast and convenient way for active isolation [17]. The merits of the hardware used for active compensation for reducing the coupled transmit noise is demonstrated.

3.2 Theory

3.2.1 Signal Description in STAR

With the inclusion of the self-interference, acquired signal $s_{\mathrm{Rx}}(t)$ can be described as in Eq. (3.1).

$$s_{\mathrm{Rx}}(t) = s_{\mathrm{MR}}(t) + n_{\mathrm{acq}} + A(t) \cdot e^{i\phi(t)} \cdot \bar{s}_{\mathrm{Tx}}(t) \tag{3.1}$$

Here, $\bar{s}_{\mathrm{Tx}}(t)$ is the distorted transmit pulse mainly leaked due to the coupling effect between the transmit and receive coil. It can be further expanded as $\bar{s}_{\mathrm{Tx}}(t) = s_{\mathrm{Tx}}(t) + \varepsilon + n_{\mathrm{Tx}}$, where $s_{\mathrm{Tx}}(t)$ is the ideal RF pulse, ε is the spurs (or spurious tones originating from the quantization errors in digital frequency synthesis) and distortions added to the pulse and n_{Tx} is the transmit noise. $A(t)$ and $\phi(t)$ are time-varying amplitude and phase modulations on $\bar{s}_{\mathrm{Tx}}(t)$ occurring due to load variations, temperature change, vibrations, etc. n_{acq} is the receive noise, which in pulsed MRI is the only noise source in the system. It will remain even if the other noise sources in the STAR imaging is eliminated.

3.2.2 Noise and Spurs

The general strategy on STAR imaging in MRI is to isolate the transmit and receive coils on the analog domain as much as possible and then remove residual leak signal during image reconstruction by utilizing digital subtraction methods. Having higher isolation is beneficial in terms of increased dynamic range and reduced artifacts that stem from imperfect digital subtraction. Although achieving isolation high enough to suppress the leak below the noise floor is theoretically possible, preserving this isolation throughout imaging is not always feasible. Hence, having a metric to determine sufficient isolation to achieve the desired SNR value is essential, especially for designing hardware for active cancellation.

In the case of STAR imaging, the dominant noise sources can be listed as white noise that is mostly stemming from the thermal noise of transmit chain elements [49], the phase noise primarily originating from the signal synthesizer of the spectrometer and further emphasized by the the devices that have non-linear behavior [50, 51, 52], spurs that consist of undesired frequency peaks arising from external interference coupled to transmit path and the quantization process of the spectrometer [53].

In conventional imaging, in the absence of the noise sources above, received noise power at room temperature, which corresponds to the noise level at the output of the receive chain (also corresponds to the power spectral density of n_{acq} from Eq. (3.1)) will be close to the noise floor and can be written as:

$$N_{\mathrm{acq}} = k \cdot T \cdot F_{\mathrm{Rx}} \cdot G_{\mathrm{Rx}} \tag{3.2}$$

Here, G_{Rx} and F_{Rx} are the overall gain and noise figure of the receive chain, respectively. k is the Boltzmann constant, and T is the temperature of the body. This quantity can also be considered the minimum achievable noise power density for STAR imaging, i.e., the noise level of conventional imaging. If the noise sources coming from the transmit chain are reduced to this level, the acquisition noise floor becomes dominant, and it is not necessary to further increase isolation for noise purposes.

To understand the relationship between the transmit parameters and SNR, it is assumed that the transmit chain noise at the output of the STAR circuit is perfectly correlated to the transmit chain noise at the output of the receive coil, i.e., the amount of cancellation achieved for the signal is also the amount of cancellation achieved for the noise. Also, it is assumed that no other noise is coupled to the system after the transmit chain. Failure of these assumptions will result in an underestimation of the noise power. With these assumptions, the total received noise N_{sys} can be calculated as:

$$N_{\mathrm{sys}} = N_{\mathrm{acq}} + ((N_{\mathrm{Tx}} \cdot G_{\mathrm{isol}} + N_{\mathrm{STAR}}) \cdot G_{\mathrm{LNA}} + N_{\mathrm{LNA}}) \cdot G_{\mathrm{Rx}} \tag{3.3}$$

$$N_{\mathrm{Tx}} = N_{\mathrm{Spec}} \cdot G_{\mathrm{PA}} + N_{\mathrm{PA}} \tag{3.4}$$

The magnitude of total isolation obtained by the combination (sum of the complex gains) of the coil's isolation and vector modulator's output is denoted as G_{isol}. Here, G_{PA}, G_{LNA}, and G_{Rx} are the gain (or attenuation) of the transmit power amplifier (PA), the low-noise amplifier (LNA), and the rest of the receive chain respectively. Similarly, N_{Spec}, N_{PA}, N_{STAR}, and N_{LNA} are the output referred noise power of the spectrometer, the transmit amplifier, the vector modulator, and the LNA, respectively. Observing Eq. (3.2) and (3.3), thermal noise floor kT can be chosen as a threshold to eliminate the effect of the transmit noise on the image.

$$G_{\mathrm{isol}} = \frac{kT}{N_{\mathrm{Spec}} \cdot G_{\mathrm{PA}} + N_{\mathrm{PA}}} \tag{3.5}$$

As expected, sufficient isolation is directly related to the multiplication of the spectrometer's noise output (i.e., input noise) and gain, as well as the noise output of the amplifier. Although not shown in the equation, gains (and possibly noise power spectrum due to the filters employed in the scanner) are dependent on the frequency, hence play an essential role. Considering bandwidth of the G_{isol} is quite narrow (7 kHz for -80 dB bandwidth), sufficient isolation needs to be determined by the lowest isolation in the imaging bandwidth. Thus, imaging bandwidth is also a parameter here.

3.2.3 Signal Equation

Following Bloch equation, small-tip angle approximation and general signal equation given in section 2.2, signal equation for the STAR is derived.

Since $\omega_1(s)$ is finite in time and only non-zero for $0 \leq t \leq T$ for RF pulse duration T, signal equation can be further expanded:

$$s(t) = i \int_{-\infty}^{\infty} M_0(t,r) e^{-i\omega(r)t} \int_{-\infty}^{\infty} \omega_1(s) u(t-s) e^{i\omega(r)s} ds dr \tag{3.6}$$

Rearranging the integrals:

$$s(t) = i \int_{-\infty}^{\infty} \omega_1(s) u(t-s) \left(\int_{-\infty}^{\infty} M_0(r) e^{-i\omega(r)(t-s)} dr \right) ds \tag{3.7}$$

Note that, integral on the inside resembles a 1D Fourier integral for the variable $k(t) = \gamma G_r r t$. Using this property:

$$s(t) = i \int_{-\infty}^{\infty} \omega_1(s) u(t-s) \mathcal{M}_0(k(t-s)) ds \tag{3.8}$$

where $\mathcal{M}_0(k(t))$ is the 1D Fourier transform of the $M_0(r)$.

It can also be seen that this integral is a convolution integral, hence it can be written as:

$$s(t) = i[\mathcal{M}_0(k(t))u(t)] * \omega_1(t) \tag{3.9}$$

Here, $\mathcal{M}_0(k(t))$ corresponds to one spoke of k-space and it is the desired value. Since $\omega_1(t)$ is known and $s(t)$ is acquired, $\mathcal{M}_0$ can be calculated in frequency domain as following[28, 48]:

$$\mathcal{M}_0(k(t))u(t) = \mathcal{F}^{-1} \left\{ \frac{S(f)}{i\Omega_1(f)} \right\} \tag{3.10}$$

where $\mathcal{F}^{-1}$ is the inverse Fourier transform, $S(f)$ and $\Omega_1(f)$ are the Fourier transforms of $s(t)$ and $\omega_1(t)$ respectively. To reduce noise amplification due to the deconvolution, instead of directly using this method, Wiener deconvolution is utilized, which gives minimum root-mean-squared (RMS) error if the noise spectrum of the signals are known.

From Eq. 3.10, it can be seen that only a single-sided spoke ($k(t) \geq 0$) can be acquired under the constant gradient assumption. This result is intuitive because, during STAR, there is no time in between RF pulse and acquisition to traverse the k-space. Spokes with different directions have to be acquired to fill out the rest of the k-space, i.e., the direction of r needs to be swept by adjusting the gradient amplitudes G_x, G_y, and G_z at each acquisition repetition (TR). Hence, after acquiring many spokes in different directions, and after the deconvolution process, an inside out radial trajectory is obtained.

3.3 Methods

3.3.1 Hardware

The hardware consists of a vector modulator [33] and Wilkinson Divider/Combiners to sum the modified transmit signal with the received signal. The combined signal at the output of the Wilkinson Combiner is measured via scanner and sent to a remote computer, where the cancellation algorithm resides. Cancellation codes (inputs of the vector modulator) determined by the remote computer are sent to a mini-computer (Raspberry Pi 3B+) placed in the scanner room via an optical link that translates the inputs into SPI protocol to program the attenuators in vector modulator. A detailed schematic of the overall system is given in Fig. 3.1.

3.3.1.1 Vector Modulator

Vector modulators are used to control the phase and amplitude of a signal. There are several different ways to implement vector modulators depending on the application and specifications (i.e., frequency range, linearity, power, and noise requirements) [40, 41, 42]. In this work, the vector modulator is implemented from discrete components to satisfy the relatively high power requirement (¡20 dBm),

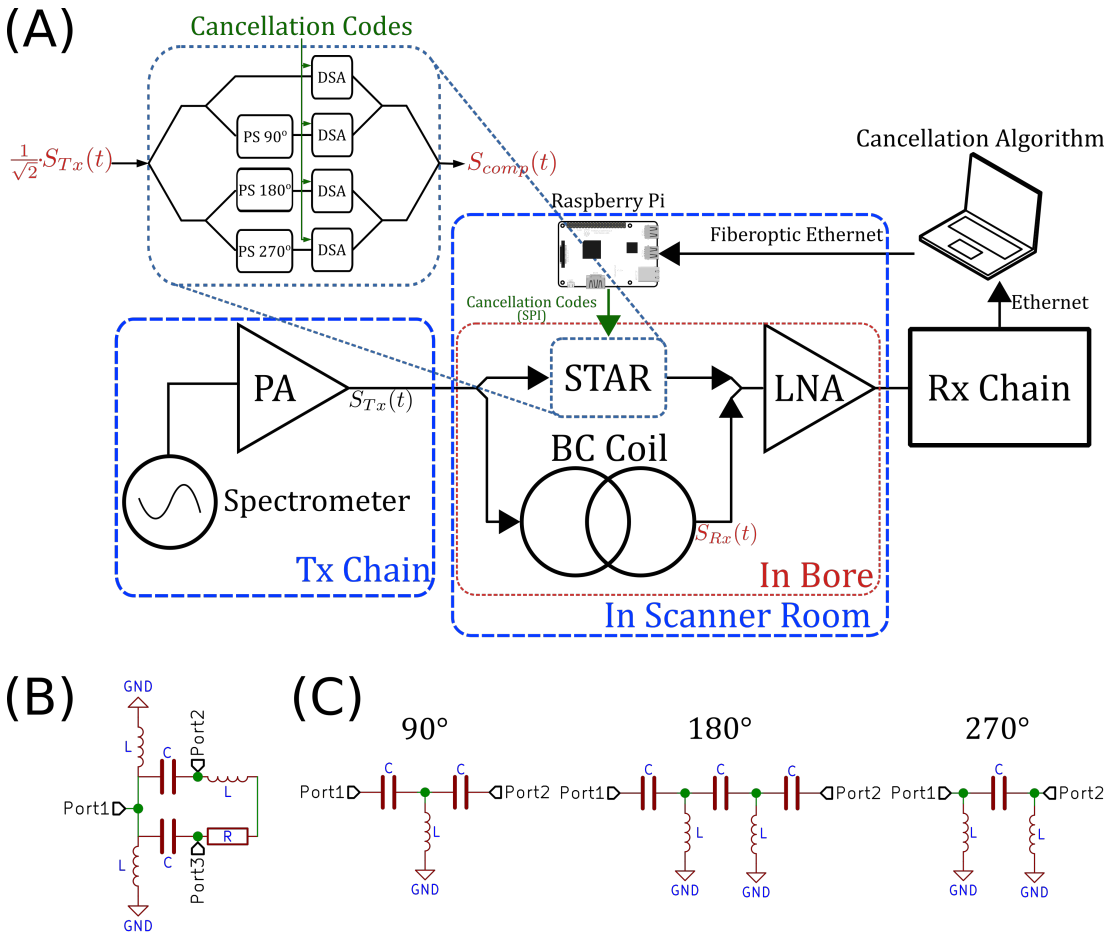

Figure 3.1: Schematic description of the STAR system and the MRI scanner. **(A)** Overall system diagram. Measurements are read from the scanner after digitization via real-time data transfer functionality. **(B)** Implementation of the Wilkinson Power Divider/Combiner as proposed in Okada et al. [1]. **(C)** Implementation of the fixed phase shifters.

low-frequency regime (123 MHz), and low noise contribution. The structure is similar to the structure in Bharadia et al. [37] with 4-phase branches. The number of active elements is kept minimum to reduce noise contribution. In each branch, the amplitude is controlled by digital step attenuators (DSA). Each branch adds a distinct fixed phase to cover the different parts of the complex plane, together with the amplitude control. These branches can be thought of as forming basis vectors that span the complex plane. In our implementation, four branches with a 90°phase difference are used to provide adequate coverage of the complex plane.

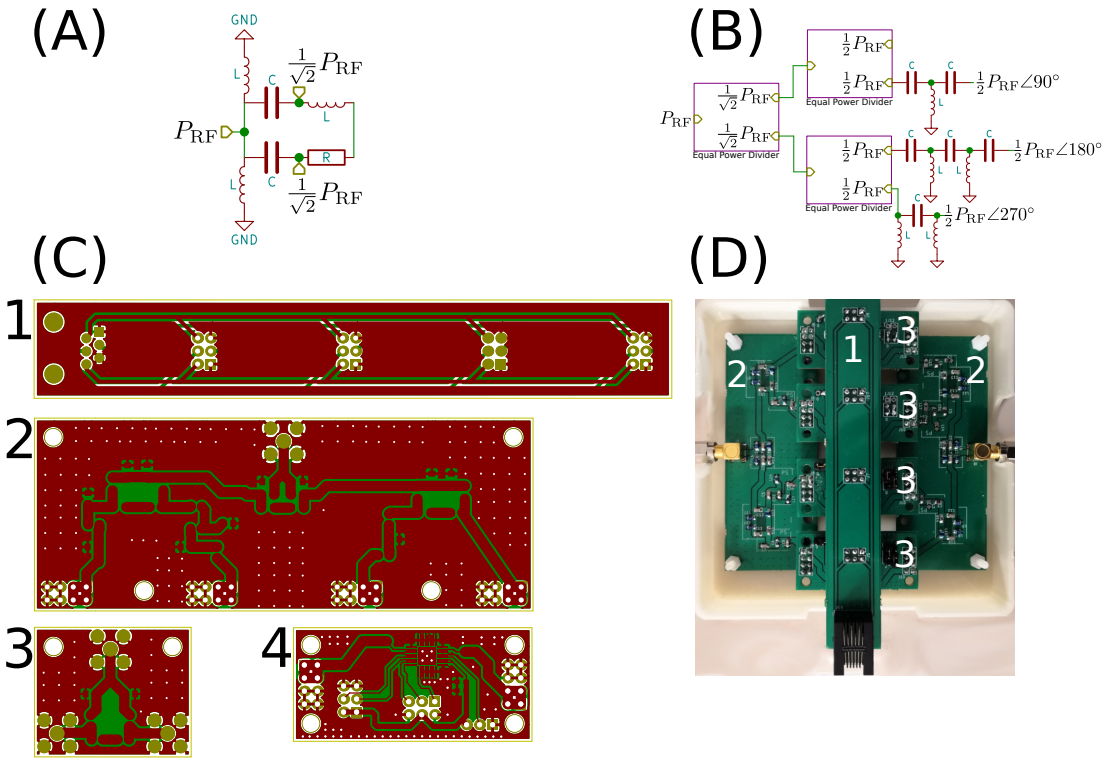

Figure 3.2: **(A)** Schematic of the Equal Wilkinson Power Divider. If unequal power division is desired, additional matching circuitry is required after the division ports. **(B)** Schematic of the 4-way divider and fixed phase shifters. Fixed phase shifters are only implemented in the division part. At the combiner part, necessary places are bypassed via shorting. **(C)** PCB layouts of the circuits. 1- Connector module that distributes power and control signals to the attenuators. 2- Layout of the circuit at (B). 3- Layout of the Equal Wilkinson Divider in (A). 4- Layout of the attenuators. **(D)** Image of the vector modulator. Parts are annotated according to the numbers in (C).

RF signal is divided into the branches via Wilkinson power dividers/combiners. After phase shift and attenuation, signals from each branch are combined back by the same Wilkinson divider/combiner topology.

For ease of use and future extensions, the circuit is designed in a modular fashion. Three Wilkinson divider/combiners are designed on the same PCB and used to divide the input signal into four and phase-shifting if necessary and combine the output of each branch after attenuation. In between the combiner/dividers, each attenuator is connected as separate modules. In this way, in the future, the number of branches can be doubled by simply connecting the modules in parallel.

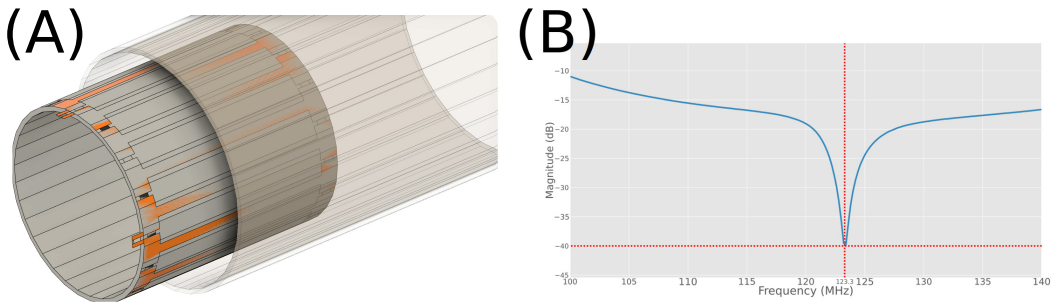

Figure 3.3: **(A)** 3D Model of the birdcage coil. The outer cylinder is the shield, and it is shifted to reveal the coil frame. The coil frame can be seen as the inner cylinder, and the copper parts and ports are visible. **(B)** S-parameter measurements of the constructed coil. 40 dB isolation is achieved at the center frequency. Isolation is more than 30 dB in a 1 MHz bandwidth around the center frequency.

Detailed schematics are given in Fig. 3.2.

The equations necessary to calculate the component values for Wilkinson dividers and phase shifters are given in the Appendix A. Calculated lumped element values along with the s-parameters of the attenuators from the manufacturer and s-parameter measurements of the coil are used to simulate the circuit and its isolation performance in AWR Microwave Office.

In the ideal case where there is no reflection between the stages of the circuit, and there is infinite isolation between the dividing branches of the dividers, the output of the vector modulator is simply the complex sum of each branch, multiplied by the complex attenuation factor that is determined by the current state of the attenuators. In this work, this assumption will be used to estimate the output of the circuit. Failure in this assumption is not critical since it has the same effect as the coupling between the coils and results in a higher residual signal than expected. This is the leading cause of the cancellation error and can be corrected with the same circuit via the proposed algorithm.

In this work, the inherent electrical isolation between the ports of the birdcage coil are exploited for passive isolation. Birdcage coils are widely used and well known in the MRI community. Usually, they are quadratically driven to achieve

field homogeneity, i.e., ports are driven with the same signal, but one port has a 90°phase shift. For our case, one port was used to transmit while the other port was used for receiving. As a result, the coil is linearly driven.

The coil is designed for knee imaging and simulated using HFSS. It is drawn as a PCB in KiCAD design software. It is fabricated on a flexible PCB sheet and fixed onto a plexiglass cylinder with proper diameter. The capacitors are placed according to the simulation. Variable capacitors are placed as tuning capacitors just below the ports, and the coil is manually tuned after the shield is placed. The shield is made of thin copper sheets wrapped around another plexiglass. The copper sheets are slit and connected via capacitors to avoid the eddy current induction on the shield due to the gradients. The isolation between the ports is measured between 30 dB and 40 dB, depending on the load. The design of the coil and the S-parameters measurements can be seen in Fig. 3.3.

A custom-made two-port 16-rung high-pass birdcage coil is used as a transceiver with around -20 dB reflection at the ports and less than -35 dB coupling between its ports. For power division and combination, topology proposed by Okada et al. [43, 1] is used, due to its relatively flat frequency response. This topology provides around 0.5° phase variation and less than 0.1% amplitude variation over 1 MHz bandwidth around the center frequency of 123 MHz.

3.3.2 Imaging Experiments

All experiments were conducted on a 3T Siemens Tim Trio scanner (Siemens Medical Solutions, Erlangen, Germany). The imaging sequence consisted of the calibration and imaging parts. The calibration part ran first and sampled the leakage by simultaneously transmitting and receiving. After the predetermined isolation threshold was surpassed, the image was acquired similar to the cSWIFT sequence. For excitation, Tukey windowed chirp pulse was used [29]. Gradients were not ramped down after the acquisition, both to reduce acoustic noise and vibrations due to gradient switching, and to crush the remaining signal before the next TR. For 3D sequences, the cancellation loop was automatically repeated

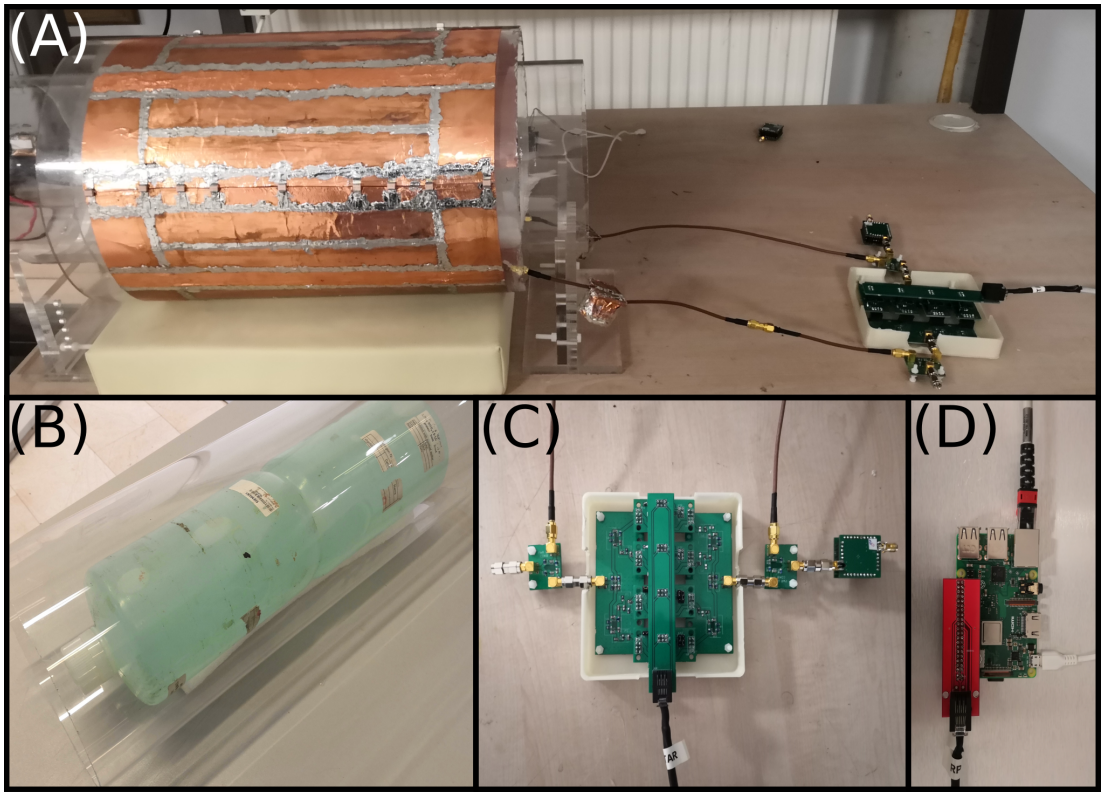

Figure 3.4: Photographs of the experiment setup. **(A)** Overall experiment setup. **(B)** Imaging phantoms and their placements in the coil. **(C)** Vector modulator. Circuit is connected to the coil, the power low-noise amplifier (PLNA) and the LNA via Wilkinson Power Dividers/Combiners. **(D)** Raspberry Pi 3B+ communicates and powers the vector modulator.

after every 2D projection to keep the isolation below the threshold throughout imaging. Number of samples per line is chosen as $N = 256$ with $FOV = 30$ cm to have an acceptable resolution and scan time, which amounts to approximately 205887 spokes to satisfy Nyquist criterion. However, 65536 spokes are acquired (256x256x256 matrix size), which yielded acceptable image quality.

Circuit characterization measurements were also acquired with the scanner to show that it is also possible to characterize the circuit when no network analyzer is present or without the need to disconnect the circuit from the coil, which is especially convenient for future clinical applications. However, special care must be taken not to acquire MR signal during characterization (e.g., crushing the signal with high gradients).

For the transmit RF pulse, power was set to 25 mW regardless of the pulse duration. Flip angle was estimated as 2° ms^{-1} by averaging over a region of interest in the middle of the phantom using a simulated B_1 map of the birdcage coil.

Two jar-shaped $CuSO_4$ phantoms (Siemens Medical Solutions, Erlangen, Germany) were placed in the birdcage coil so that their bottoms are barely touching to each other, as can be seen in Fig. 3.4-B. This placement was done to load the coil and mimic the knee since the coil is designed for knee imaging. It was attempted to place the middle of two phantoms at the isocenter by adequately positioning the coil inside the bore. FOV was set to 300 mm in the radial direction, which was enough since the imaging bandwidth was low, there was not much signal coming from the low T_2 materials including the coil frame, and only the phantoms were signal sources.

3.3.3 Image Reconstruction

Image reconstruction was performed by first deconvolving, then applying bullseye filtering as described by Corum et al. [44]. Deconvolution is performed in the frequency domain by Wiener deconvolution. For the noise spectrum, white Gaussian noise is assumed, and the spurs and residual transmit signal are omitted in the deconvolution process. The noise power is estimated via inspection of the acquired data. Note that one can compromise from resolution to reduce noise and artifacts from the final image by considering the effect of spurs and residual. Finally, deconvolved and filtered radial k-space data was reconstructed to the 3D volume via gridding [15] and inverse Fourier transform.

Reconstruction algorithms are implemented in MATLAB. Code can be viewed at `https://gitlab.com/btasdelen/star-mri-reconstruction`.

3.3.4 Deconvolution

As mentioned before, Wiener deconvolution is used after the Eq. (3.9) instead of the Eq. (3.10) since it is more resilient to noise. Eq. (3.9) can be rewritten if noise term is added and step function is omitted:

$$s(t) = i\mathcal{M}_0(k(t)) * \omega_1(t) + n(t) \tag{3.11}$$

To find an estimate $\hat{\mathcal{M}}_0(k(t))$, some $g(t)$ can be found such that $\hat{\mathcal{M}}_0(k(t)) = -ig(t) * s(t)$. Here, $\hat{\mathcal{M}}_0(k(t))$ is an estimate of $\mathcal{M}_0(k(t))$ in the sense that it minimizes the mean squared error. The Wiener deconvolution filter that satisfies this equation can be given as:

$$G(f) = \frac{\Omega_1^*(f)S_{\text{psd}}(f)}{|\Omega_1(f)|^2 S_{\text{psd}}(f) + N(f)} \tag{3.12}$$

Here, $G(f)$ and $\Omega_1(f)$ are the Fourier transforms of $g(t)$ and $\omega_1(t)$ respectively. $S_{\text{psd}}(f)$ and $N(f)$ is the mean power spectral density (PSD) of the signal $s(t)$ and noise $n(t)$ respectively. Hence, $\hat{\mathcal{M}}_0(k)$ can be found as:

$$\hat{\mathcal{M}}_0(k) = -i\mathcal{F}^{-1}\{G(f)S(f)\} \tag{3.13}$$

where $S(f)$ is the Fourier transform of $s(t)$ and $\mathcal{F}^{-1}$ is the inverse Fourier transformation operator.

As $\omega_1(t)$ corresponds to the ideal excitation pulse, and ideally, it is known. In this study, due to the hardware distortions of the excitation pulse related to the timing, ring-like (bullseye) artifacts are observed on the image. These distortions are corrected manually by adjusting the timing of the $\omega_1(t)$.

PSD of the noise term ($N(f)$) is also required to calculate the $G(f)$. Here, noise is assumed to be white noise, and its mean power is estimated by the inspection of the background noise to the signal in acquired spokes. Note that,

instead of assuming white noise, noise statistics for the imaging system in the imaging bandwidth (noise spectrum) can be obtained and used to yield better image quality.

Matlab implementation of the Wiener deconvolution is given at `https://gitlab.com/btasdelen/star-mri-reconstruction`.

3.3.4.1 Filtering

After the deconvolution process, the data can be filtered to reduce noise and artifacts. In this work, an essential filter is the bullseye filter as described by Corum et. al. [44]. Although the the bullseye filtering benefits are more prominent in STAR MRI, it is applicable for all radial k-space trajectories.

In radial imaging, unlike the Cartesian trajectories, inaccuracies in gradient timings, RF pulse, and k-space trajectory affects the image in an angle consistent way, which amplifies the resulting artifacts on the image compared to the Cartesian trajectories. However, this angle consistency can also be exploited to reduce these artifacts. Steps to apply this filter is as follows:

1. Let $H_i(f)$ be the Fourier transform of the ith k-space spoke $h_i(t)$ after the deconvolution process. Take the mean of every acquired spoke, so that $\bar{H}(f) = \sum_{i=1}^{N_s} H_i(f)/N_s$.
2. Calculate $\bar{\bar{H}}(f)$ by filtering the $\bar{H}(f)$ with a sharp window; a Hamming window power to the 30 in this case.
3. Calculate the corrected spokes by $H_{\text{corr}} = H_i(f)\frac{\bar{\bar{H}}(f)}{\bar{H}(f)}$ for every i.

These steps can be repeated multiple times to further reduce the artifacts; however, the return is diminishing. In this work, applying the filter twice is observed to remove most artifacts, and further filtering did not result in a significant improvement. The effect of the filter can be seen in Fig. 3.5.

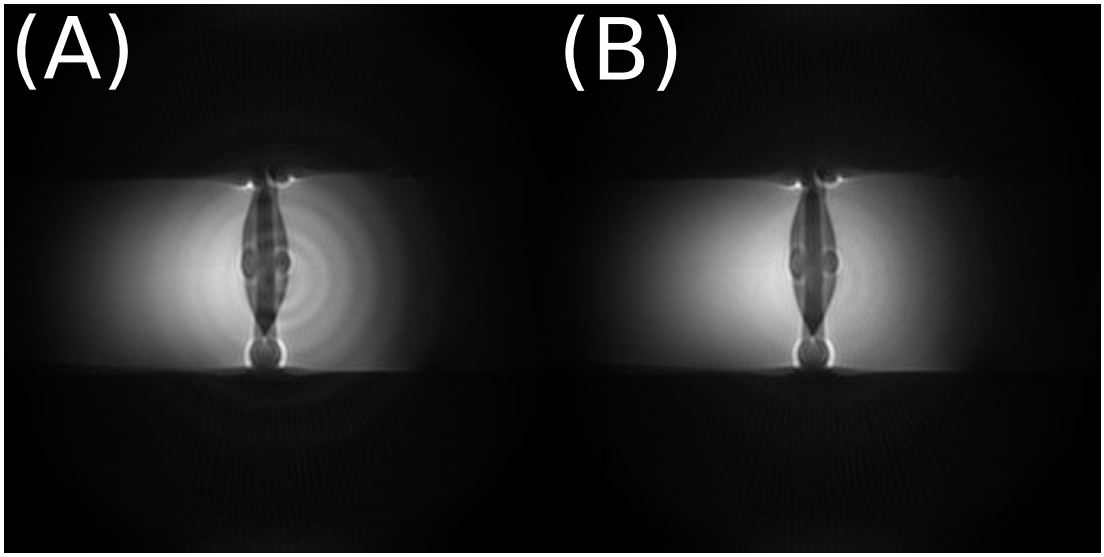

Figure 3.5: Image before **(A)** and after **(B)** the bullseye filtering. In (A), more ring-like artifacts are visible compared to (B). No distortion is observed on the image due to the filtering. It can be seen that, the bullseye filtering does not reduce the artifacts caused by other sources, such as susceptibility.

Apart from the bullseye filtering, gradient timing correction [45] and, susceptibility correction [46] can also be applied afterward. Although these methods are implemented, they are not detailed in this work since no significant improvement is observed in the image quality.

Matlab implementation of the bullseye filtering is given at `https://gitlab.com/btasdelen/star-mri-reconstruction`.

3.3.5 Noise Experiments

For noise experiments, the noise power density at the output of each component was estimated. Noise contributions were investigated as output referred noise power N, which can be calculated in terms of noise figure F and gain G of the device under test (DUT).

Output referred noise power was inferred from the measurements to characterize the receive system using the same pulse sequence used with imaging. 10 ms

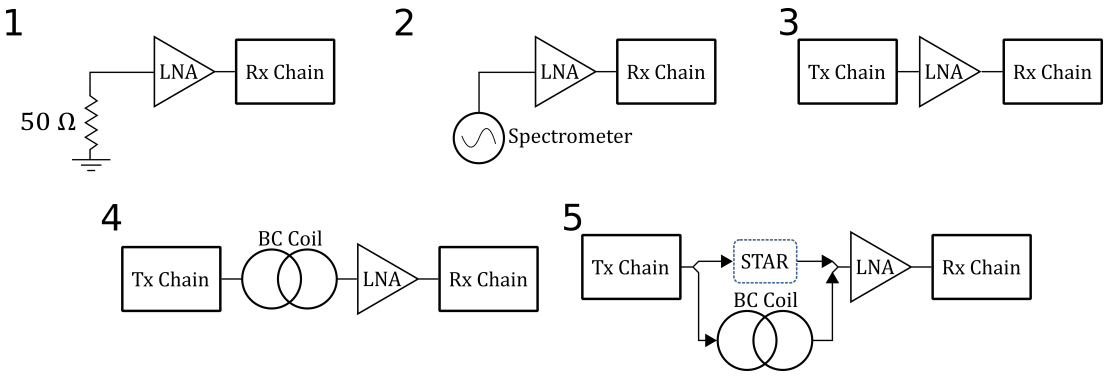

Figure 3.6: Schematics of the noise experiments. Experiments 3, 4 and 5 are repeated for power low-noise amplifier (PLNA), cascaded power low-noise amplifier ($PLNA^2$), and Analogic transmit power amplifier (ATPA). An attenuator of known value after the transmit chain is used when necessary to protect receive chain from saturation and damage.

long rectangular RF pulses were sent, and received signal was acquired simultaneously. Gains were measured similarly. The measurements were done according to the modeled experiments in Fig. 3.6. Attenuators with known values were used as necessary to keep the amplitude of the received signal in the receiver's dynamic range. TR was set as 20 ms, which amounts to an RF duty cycle of 50%, in order to avoid amplifier errors. The sampling rate of the analog-digital converter was 200 kHz, which amounts to 2000 samples during RF. Several TRs are concatenated to increase the number of samples. The patient table was kept outside of the bore during the noise experiments in order not to acquire the MR signal. The experiments were repeated four times to verify the results. Power spectral density (PSD) of the concatenated data was calculated to assess the noise in the spectrum.

In the noise experiments, three different transmit amplifier combinations were used. The first amplifier, which was referred to as a power low-noise amplifier (PLNA) in this paper, was custom-designed using a PLNA chip (GRF5020, Guerilla RF). The chip has around 29 dB gain and OP1dB of 27 dBm. The second setup was called as $PLNA^2$, and it was the cascade of two PLNA, which amounts to 59 dB gain and OP1dB of 27 dBm. The last amplifier, referred to as Analogic transmit power amplifier (ATPA), was the transmit array amplifier of the scanner (AN8135, Analogic), which had around 69 dB of gain and 8 kW peak

power output. A network analyzer (E5061B, Agilent) and a noise figure meter (8970B, HP) were used for gain and noise figure measurements.

3.4 Results

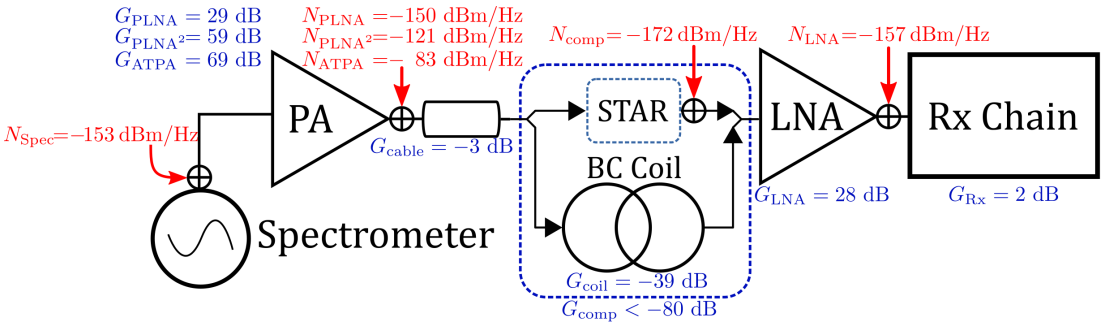

Figure 3.7: Gains and output referred noise powers are annotated on the system schematic. Gains and noise spectral density of PLNA, PLNA^2, and LNA, as well as gain of the coil and noise spectral density of the vector modulator is measured with a network analyzer and noise figure meter, and also verified with scanner measurements.

Measured output referred noise powers, and gains of the blocks can be seen in the schematic in Fig. 3.7. All the values are verified by repeating the measurements and experiments four times on different days.

White noise measurements when no RF power is present can be seen in Table 3.1. These measurements are also verified with the measurements in the presence of RF power. Measurements are in good agreement with calculated values for PLNA. However, for PLNA^2 and ATPA, the measurements have deviated from the calculated values for experiments 4 and 5.

Lastly, the PSD of the experiments can be seen in Fig. 3.8. Spurs, phase noise, and leak signal isolation behaved as expected. However, as mentioned above, background noise was not reduced to the expected level.

Acquired images with the system can be seen in Fig. 3.9. Bullseye artifacts stemming from the RF and the radial sampling imperfections were mostly reduced

	Experiment	Calculated (dBm/Hz)	Measured (dBm/Hz)
	1	-144	-144.2
	2	-126	-126.2
	3	-97	-96.5
PLNA	4	-135	-134.9
	5	-140	-138.6
	3	-67	-67
PLNA²	4	-106	-112.2
	5	-140	-115.3
	3	-54	-54.6
ATPA	4	-93	-92.7
	5	-137	-106.6

Table 3.1: Noise spectral density for the Larmor frequency for each experiment. Noise measurements are acquired when RF voltage is set to 0 Volts. For verification, these measurements are compared to the background noise level with the experiment when RF power is present.

with bullseye filtering. Visible disturbances on the signal occurred due to the vibrations were eliminated by adding a dead time after gradient switching.

Images with 2.56 kHz bandwidth suffered from susceptibility artifacts but exhibited fewer artifacts due to residual leak signal. Also, artifacts were more prominent at the middle slices, whereas in the periphery, they diminished. Furthermore, the number of spokes was halved for low bandwidth images since scan time was prohibitively long. Thus, streaking artifacts occurred due to undersampling.

Additional bullseye artifacts were observed in the images due to the timing issue of the RF pulse, which was also seen on raw data. The duration of the intended RF pulse and the actual RF pulse were different. This difference was corrected by stretching the RF pulse in time while the middle part is stationary. Then, the modified RF pulse was used in deconvolution, which eliminated these bullseye artifacts.

3.5 Discussion

In STAR imaging, transmit noise also plays a vital role in determining the SNR. Transmit noise can be considered as the noise input to the transmit system (generated by spectrometer) multiplied by the transmit gain and the additional contributions of other noise generating elements (amplifiers and the cancellation circuit) as summarized in Eq. 3.3. With proposed cancellation hardware, it is shown that it is possible to isolate the transmit noise in addition to the leak signal for a given transmit gain.

Following the relationship between isolation, noise, and transmit chain parameters given in Eq. 3.5, sufficient isolation can be calculated to reduce the noise to the receive noise level or minimum achievable noise level. Minimum possible noise is emphasized as the threshold since it eliminates the SNR disadvantage of STAR over the conventional imaging. After reducing the excess noise, digital subtraction methods can be used in post-processing to remove the residual leak.

Isolation can be further increased to recover the reduced dynamic range and suppress the artifacts due to the imperfect digital subtraction. With higher possible isolation, higher gain amplifiers (e.g., the system's amplifier) can be used for STAR imaging without losing SNR. This trade-off is essential since switching the transmit amplifier is inconvenient, more so for clinical applications. Furthermore, using higher gain without increasing additive noise due to the transmit chain may enable a higher flip angle, which in turn, can yield better SNR. On the other hand, reducing sufficient isolation can also be preferred in some applications to reduce the circuit complexity and cost, as well as the algorithm memory consumption. A lower gain transmit amplifier can be used, or a spectrometer with lower noise output can be used to relax the required isolation.

From Eq. 3.5, it can be seen that reducing amplifier noise output also reduces sufficient isolation. However, unless the noise output of the transmit amplifier is comparable to the spectrometer noise amplified by the transmit amplifier gain,

it will not be the dominant factor determining the sufficient isolation. This conclusion implies that there is no need to invest in a low noise amplifier for the transmitter, whereas the amplifier's gain plays an important role.

In noise experiments, although the spurs, phase noise, and leak signal are isolated, white noise is not reduced to the expected levels, with $PLNA^2$ and ATPA. Additional experiments suggest that the reason is an external white noise source coupled through coils. Although the source of this noise seems to be the transmit path, it could not be eliminated. The noise coupled to the receive coil does not follow through the cancellation path; hence, it does not share the strong noise correlation property with the cancellation signal. Although the power of this noise source is quite small, it still detriments the SNR significantly. The exact cause of this noise source needs further investigation. However, it is expected that rigorous shielding and usage of more cable traps should ameliorate the issue.

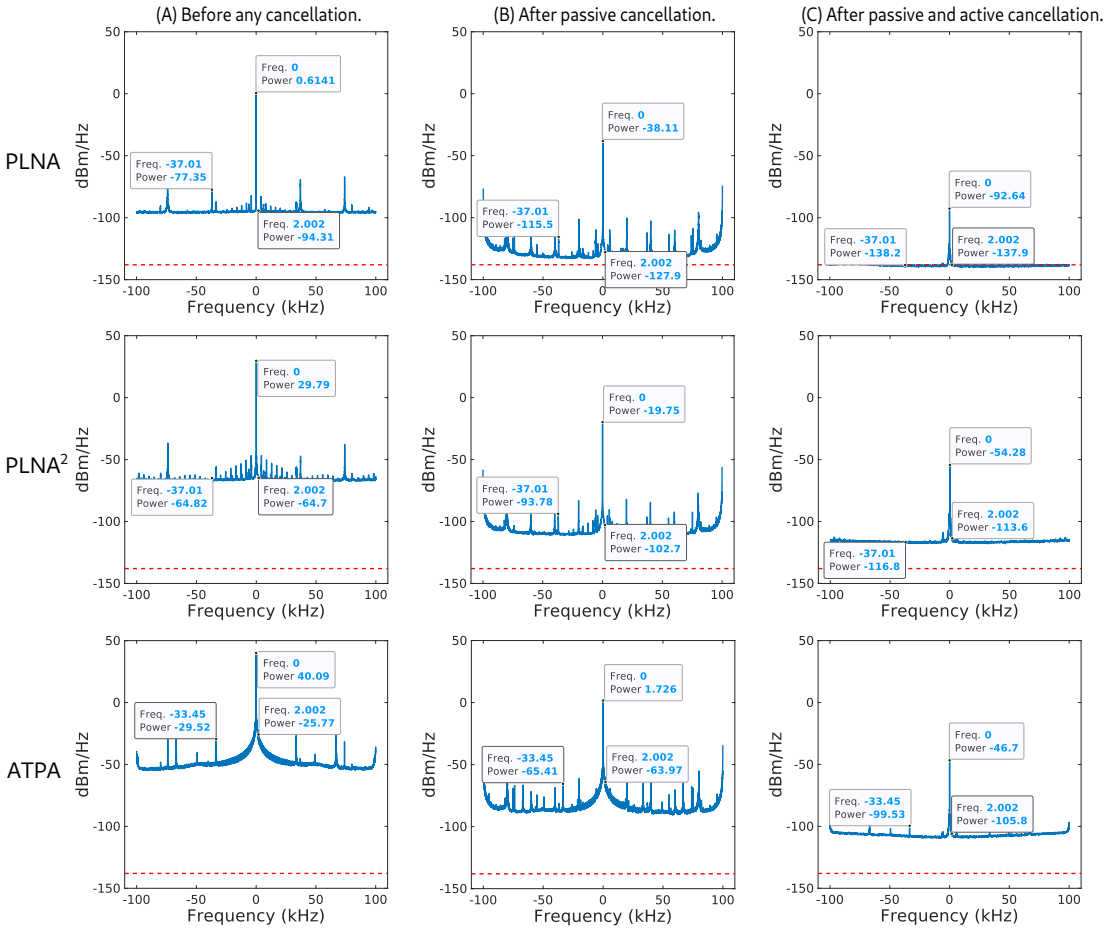

Figure 3.8: Noise PSD for three noise experiments (experiments 3, 4 and 5) and amplifiers PLNA, PLNA^2, and ATPA. Red dashed line marks the minimum achievable noise level. **(A)** Low frequency (5.6 kHz) harmonics that can be seen in PLNA and PLNA^2 are coupling from the power supply of custom amplifiers. At ATPA, phase noise can be observed at ATPA as the spread around the center frequency. **(B)** After passive isolation (40 dB), it can be observed that both noise and spur is reduced significantly. Since thermal noise is also reduced, some peaks that were not visible became visible. **(C)** After active isolation with the isolation threshold 80 dB, most peaks are cleared out.

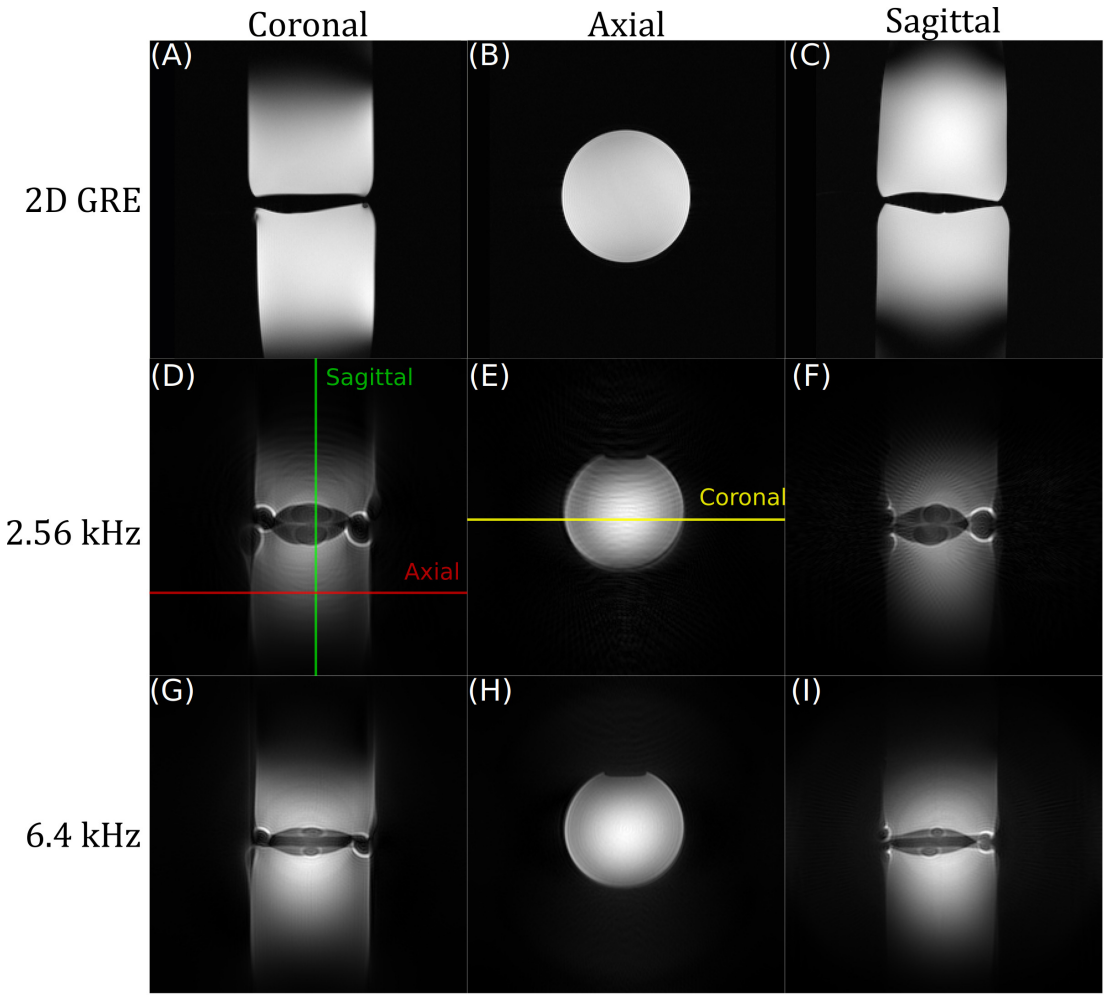

Figure 3.9: **(A) - (C)** are reference 2D GRE images with FOV 250x250 mm, 256x230 matrix size and 81.92 kHz bandwidth. cSWIFT images **(D)-(F)** acquired with 2.56 kHz bandwidth and **(G)-(I)** acquired with 6.4 kHz bandwidth.

Chapter 4

A Look-up Table Based Algorithm for Dynamic Cancellation in Simultaneous Transmission and Reception

4.1 Introduction

In this chapter, it is shown that by using an active cancellation circuit and a control algorithm, it is possible to isolate the leakage in a dynamic manner, so that even though the coupling changes over time, isolation can be kept under a threshold. This work was submitted as an abstract [17] to International Society of Magnetic Resonance in Medicine (ISMRM) 2019 and presented as a poster presentation.

In this work, a novel algorithm that can be used for dynamically canceling out the self-interference signal is proposed and analyzed. Its advantages and capabilities are demonstrated on a digitally controlled vector modulator with bench-top

and MRI experiments. Its mathematical analysis is done to understand the inner workings of the algorithm which is expected to help in future extensions and the improvements on the algorithm. It is important to note that, the proposed algorithm is by no means limited to MRI applications, in fact it can be applied other areas including full-duplex communications and MPI.

4.2 Theory

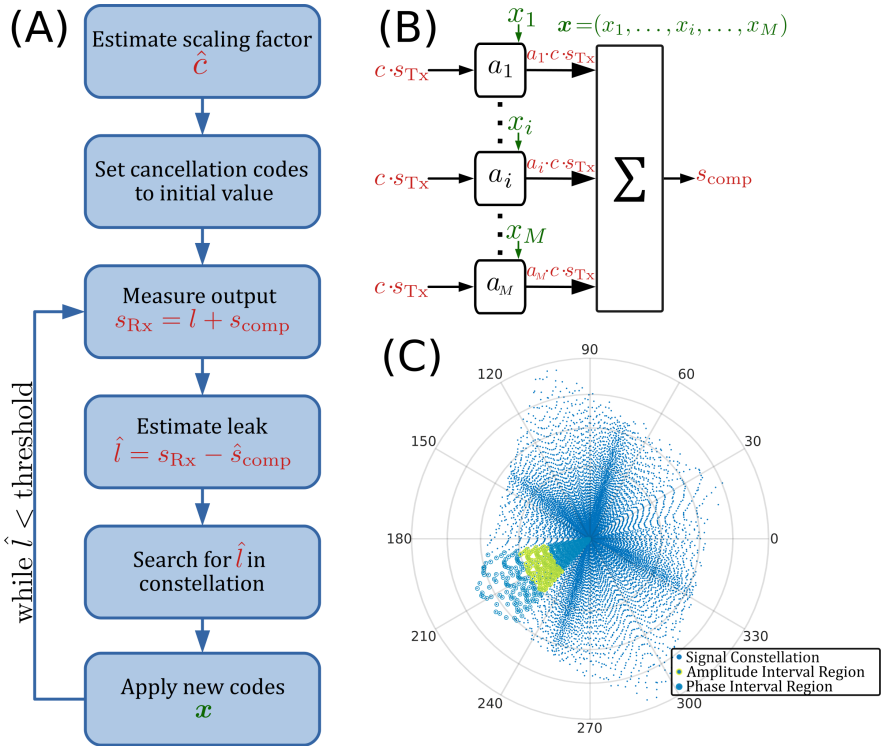

Figure 4.1: The decoupling algorithm. **(A)** Flow chart of the compensation loop. $\hat{c}$, $\hat{l}$ and $\hat{s}_{\mathrm{comp}}$ can be considered as estimated $X(f)$, $L(f)$ and $Y(f, \boldsymbol{x})$ at the center frequency respectively. **(B)** Model assumed on the vector modulator. In other terms, the output s_{comp} is the weighted combination of the input $c \cdot s_{\mathrm{Tx}}$ by the complex weight a_i of each line. **(C)** A representative visualization of the constellation. Each point represents the value of the transfer function at the center frequency for a given $\boldsymbol{x}$ vector. A subsection divided according to the phase and the amplitude can be seen as the yellow part.

The aim of the active cancellation using a vector modulator is, modifying the phase and amplitude of the signal so that, when summed up, the output should

be zero. For our vector modulator structure, that corresponds to setting digital inputs that will yield desired phase shift and attenuation. In the literature, to find the inputs that will minimize the leak signal by matching the phase and amplitude, usually searching algorithms such as gradient descent and genetic algorithms are used [32, 39]. These approaches work well, especially if the problem has a small number of degrees of freedom and does not have many local minima. For some circuits as used in Salim and Atalar [39], the problem becomes quite complex with an abundance of local minima and a high number of degrees of freedom. Convergence time drastically increases with this complexity. In both cases, reaching a good solution with fewer iterations is important since the measurement is costly. In Bharadia et al. [37], a look-up table (LUT) based algorithm is utilized, which finds a good initial point for gradient descent, increasing the convergence rate. Our approach is to extend this idea (storing the circuit behavior) by characterizing the circuit via measurements once and using this LUT to find a minimum point. Hence, it is possible to decrease further the time required to find a minimum point since the need for acquiring measurements for every subsequent input is eliminated. Thus, to enable these benefits by using the LUT instead of the measurements, the behavior of the circuit is modeled and the output of the circuit for a given control input is estimated.

With the linearity assumption, the input-output relationship of the vector modulator can be written as in Eq. (4.1) in the frequency domain:

$$Y(f, \boldsymbol{x}) = H(f, \boldsymbol{x}) \cdot X(f) \tag{4.1}$$

where the $\boldsymbol{x}$ is the control input vector to the vector modulator, $H(f, \boldsymbol{x})$ is the transfer function that is also dependent on the control inputs, $Y(f, \boldsymbol{x})$ is the output and $X(f)$ is the input. For a known initial $H(f, \boldsymbol{x_0})$, by measuring the output $Y(f, \boldsymbol{x})$, input $X(f)$ can be found. Once $X(f)$ is known, from Eq. (4.1), the output can be inferred for any $\boldsymbol{x}$, with the knowledge of $H(f, \boldsymbol{x})$.

For a leak signal $Y_l(f)$, estimated residual signal amplitude after the cancellation can be written as $\hat{\epsilon} = |Y_l(f) - \hat{Y}(f, \boldsymbol{x})|$ and the cancellation problem becomes $\min_{\boldsymbol{x}} |\hat{\epsilon}|$. Note that the expected residual signal amplitude $\hat{\epsilon}$ can be considered as

the quantization error caused by the quantized nature of $\boldsymbol{x}$. A source of error that increases the final true residual amplitude ϵ is the disparity between estimation $\hat{H}(f, \boldsymbol{x})$ and $H(f, \boldsymbol{x})$. Thus, to be able to attain high isolation (e.g., an additional 50 dB), the relative error of the estimated $\hat{H}(f, \boldsymbol{x})$ to the true $H(f, \boldsymbol{x})$ needs to be small. Estimations solely based on simulations and manufacturer-supplied information are not reliable enough. Our algorithm relies on the characterization measurements and a compensation loop that removes the bias and minimizes the error by iterating over a set of candidate points found from the LUT to circumvent this issue. If a selected candidate fails to meet the threshold, it was assumed either the coupling has changed, or our estimation of circuit output was off in the previous step. Hence the residual is estimated and a new candidate tried again until the threshold is achieved. For this thesis study, since taking care of frequency dependency of the hardware would increase the complexity, all of the measurements and estimations are done for a single frequency (f_0). This trade-off deemed fair since the frequency response of the leak signal is flat around the center frequency of the scanner.

The look-up table construction, which is referred as constellation in this work, and cancellation steps can be found below. By understanding how the cancellation works and examining the noise sources, isolation performance can be increased via tweaking the algorithm or modeling the circuit better, which in turn may improve the cancellation performance.

4.2.1 Constellation Construction

Following steps can be carried to construct constellation:

1. Each branch's input is swept from state 1 to N while the other lines kept at state 1 and S_{21} of the output is recorded. In this case the measurements can be formulated as:

$$m_i(x) = \sum_{k \neq i, k=1}^{M} a_k(N) + a_i(x) + l_{\text{cal}} \tag{4.2}$$

Here, $m_i(x)$ is the measurement of the circuit output for branch i at state x, $a_k(x)$ is the complex coefficient of branch k and l_{cal} is the coupled signal coming from the coil connected to the circuit during calibration, if any. Note that for this work, there are 128^4 set of states in total, since there are 128 states ($N = 128$) and four branches ($M = 4$). However, due to time constraints, only $128 \cdot 4$ different set of states are measured, just enough to solve the model. How the left-out measurements are estimated is explained in the step 2.

2. Complex coefficients that are not measured in step 1 to reduce the data collection time are estimated from the measured set as linear combinations of each branch. Complex coefficients in the constellation ($\hat{a}(\boldsymbol{x})$) are calculated for a circuit with M delay line and N states, and for state vectors $\boldsymbol{x} = \{x_i | x_i \in 1, \ldots, N, i \in 1, \ldots, M\}$ as given in Eq. (4.3):

$$\hat{a}(\boldsymbol{x}) = \sum_{k=1}^{M} m_k(x_k) \tag{4.3}$$

3. The constellation is sorted by the phase and it is categorized into sections where in each section phases of the coefficients are in some interval with the length of $\Delta\phi$. In this way, the initial index of these sections that contain the coefficients with the phases in $[k \cdot \Delta\phi, (k+1) \cdot \Delta\phi)$ are stored, for any k that satisfies $\frac{-\pi}{\Delta\phi} \leq k < \frac{\pi}{\Delta\phi}, k \in Z$.

4. The coefficients in each of these sections are sorted by their amplitudes separately. Similar to the previous step, they are categorized by their magnitude this time into subsections. The indices that point to the boundaries of these subsections are stored in another LUT. It will be used to jump directly to the vicinity of the estimations that have the phase and the amplitude values close to the desired signal.

In this work, the LUT was referred to as constellation, since it represents

the normalized output values that can be achieved by the circuit. Once the constellation is known, the cancellation loop can be carried out, as in Fig. 4.1.

The error sources of $\hat{a}(\boldsymbol{x})$ in the estimation are analyzed by inserting Eq. (4.2) into Eq. (4.3):

$$\hat{a}(\boldsymbol{x}) = \sum_{k=1}^{M} a_k(x_k) + K \tag{4.4}$$

$$K = (M-1) \cdot \sum_{k=1}^{M} a_k(N) + M \cdot l_{\text{cal}} \tag{4.5}$$

Following these equations, estimated coefficients can be written in terms of actual coefficients as follows:

$$\hat{a}(\boldsymbol{x}) = a(\boldsymbol{x}) + \epsilon(\boldsymbol{x}) + K + n_i \tag{4.6}$$

Note that K is a constant that adds bias to all estimated superposed signals in the constellation. $\epsilon(\boldsymbol{x})$ can be considered a distortion of the estimate or modeling error depending on the input vector $\boldsymbol{x}$, and n_i is the measurement noise coming from $m_i(x)$.

4.2.2 Cancellation Loop

Let the output measurement of the system at iteration k be $\bar{m}_k(\boldsymbol{x}_k)$, where $\boldsymbol{x}_k$ is the input vector to the STAR circuit at the iteration k. If the complex scaling factor due to the gain and phase addition of the overall system is omitted, $\bar{m}_k(\boldsymbol{x}_k)$ can be written as:

$$\bar{m}_k(\boldsymbol{x}_k) = l_k + a(\boldsymbol{x}_k) \tag{4.7}$$

where l_k is the leak signal, and $a_k(\boldsymbol{x}_k)$ is the output of the STAR circuit at iteration k.

From the constellation, an estimate of $a(\boldsymbol{x}_k)$, $\hat{a}(\boldsymbol{x}_k)$ is known. Hence, the leak signal at iteration k can be estimated using:

$$\hat{l}_k = \bar{m}_k(\boldsymbol{x}_k) - \hat{a}(\boldsymbol{x}_k) \tag{4.8}$$

For iteration $k+1$, the input vector $\boldsymbol{x}_{k+1}$ is chosen so that:

$$\hat{a}(\boldsymbol{x}_{k+1}) + q_{k+1} = -\hat{l}_k \tag{4.9}$$

where q_{k+1} is the error coming from the discrete nature of constellation, and $\hat{a}(\boldsymbol{x}_{k+1})$ is selected as close as possible to $\hat{l}_k$ to cancel out the leak signal.

If Eq. (4.7) and (4.8) are inserted into Eq. (4.9), following can be written:

$$\hat{a}(\boldsymbol{x}_{k+1}) = -l_k - a(\boldsymbol{x}_k) + \hat{a}(\boldsymbol{x}_k) - q_{k+1} \tag{4.10}$$

From Eq. (4.6), the equation can be further expanded by replacing $\hat{a}(\boldsymbol{x}_k)$ as:

$$\hat{a}(\boldsymbol{x}_{k+1}) = -l_k + \epsilon(\boldsymbol{x}_k) + K - q_{k+1} \tag{4.11}$$

By also replacing $\hat{a}(\boldsymbol{x}_{k+1})$ and reorganizing the equation:

$$a(\boldsymbol{x}_{k+1}) + l_k = \epsilon(\boldsymbol{x}_k) - \epsilon(\boldsymbol{x}_{k+1}) - q_{k+1} \tag{4.12}$$

There are two critical remarks in Eq. (4.12). The first one is, the constant error in the model coming from K cancels out during the feedback loop and does not affect the performance. The second is the residual leak, which is determined

by quantization error q and difference in the modeling error $\epsilon(\boldsymbol{x})$ in iteration k and $k-1$. In the case that this difference is zero, the algorithm needs only two iterations to converge. In the realistic case that the difference is non-zero, the algorithm iterates until this difference is smaller than the threshold. This observation suggests that a model with a smaller $\epsilon(\boldsymbol{x})$ is required to increase the convergence rate. However, although the output model used in the algorithm is not perfect, it is possible to achieve more than 80 dB isolation in this way, as can be seen in Fig. 4.3.

Implementation of the constellation creation and cancellation loop can be found at `https://gitlab.com/btasdelen/star-mri-cancellation-algorithm`.

4.3 Methods

Details of the hardware, imaging experiments and reconstruction can be found in Chapter 3. Additionally, the cancellation loop of the algorithm is implemented in the reconstruction unit of the scanner, ICE as a real-time feedback process. Communication between the external PC and the scanner is done via Ethernet connection. Sequence can be configured so that, apart from the beginning of the scan, cancellation loop could be run after every TR or every time z-gradient has changed, if the isolation drops below the threshold.

4.4 Results

AWR Microwave Office simulation results can be seen in Fig. 4.2.

Results related to isolation performance is given in Fig. 4.3. Due to the nature of the algorithm, at some iterations increase of the leak signal was observed; however, -80 dB isolation threshold was successfully achieved eventually (G_{isol} was less than -80 dB).

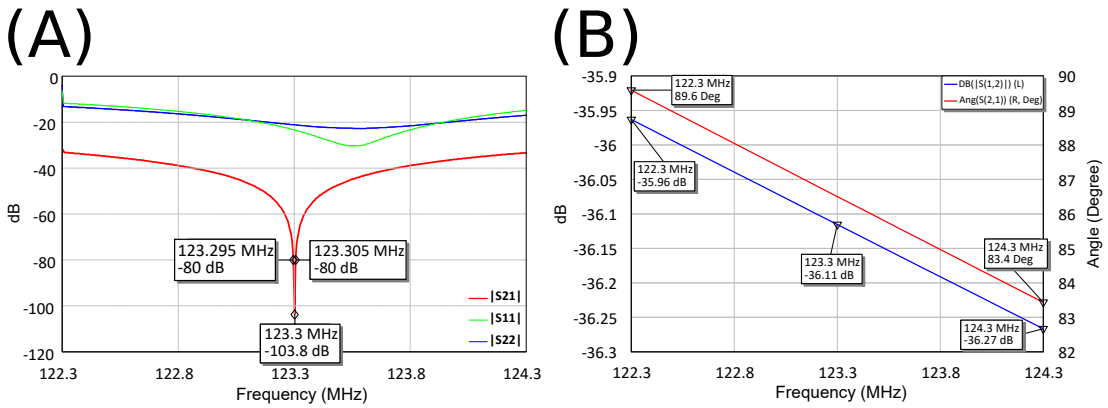

Figure 4.2: **(A)** Isolation performance with the coil measurement given in Fig. 3.3-B. -80 dB bandwidth is around 10 kHz. Digital inputs of the attenuators are optimized to minimize $|S_{21}|$ of the system. **(B)** Vector modulator S-parameters when the attenuator inputs are set as in A. The amplitude variation is around 0.3 dB and the angle variation is around 6°in 1 MHz bandwidth.

4.5 Discussion

The proposed algorithm is not exclusive to implemented vector modulator structure; it is also possible to use it for any digitally controlled system with a complicated input-output relationship (i.e., other types of non-ideal modulators). It has the advantage of reducing the number of iterations (hence the measurements) to cancel out the leak signal. It is a step towards the real-time cancellation of the time-varying leak signal. Although the algorithm is not critical for the validity of noise analysis and mitigation arguments in this work, it is of importance for the feasibility of the study.

The estimation error in the circuit output hinders the possibility of eliminating iterations. The current model, as explored above, disregards the reflections and non-linearity occurring in the circuitry. For future work, it is possible to estimate the modeling error ($\epsilon(\boldsymbol{x})$) by using several measurements with arbitrary control input ($\boldsymbol{x}$) and fitting to the error between measurement and output estimation ($\hat{a}(\boldsymbol{x})$) or directly fitting a complex non-linear function to the measurements ($m_i(x)$) itself. By eliminating iterations in this way, it will be possible to turn the cancellation process into real-time.

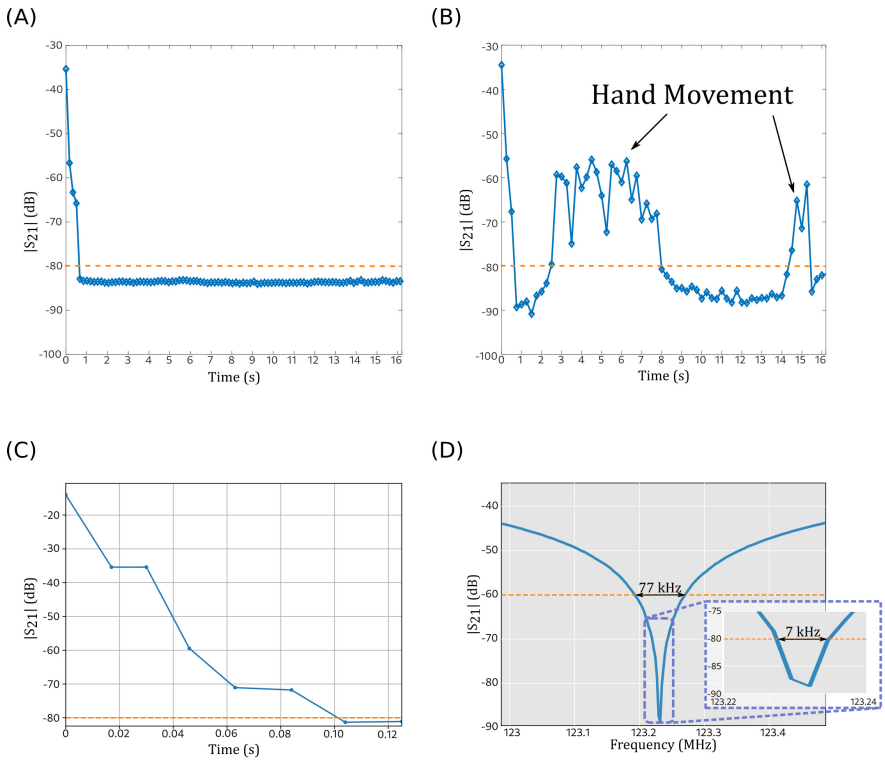

Figure 4.3: Isolation performance graphics. **(A)** Network analyzer experiment in a stable environment (e.g. load is static, no vibration around coil etc.). **(B)** Same experiment with a), but this time hand movement is present in the vicinity of the coil. **(C)** Decoupling performance in MRI scanner. Note that, due to vector modular output being higher than the leak signal, initial value for isolation does not represent passive cancellation. **(D)** G_{isol} ($|S_{21}|$) of the actively isolated system and its -60 dB and -80 dB bandwidth values.

The algorithm can be made more adaptive by employing a second receive channel to mitigate the estimation error. This receive channel can be used to measure the circuit's output through a coupler during cancellation, and the error can be corrected on the fly utilizing these measurements. This method may have two main advantages: It can capture the time-varying behavior of the circuit and eliminate the need for re-calibration over long periods. The re-calibration is required because the values of the components used in the circuit change due to temperature, moisture, etc., or the components itself may need replacements. This type of change over time reduces the performance of cancellation and is expected since the algorithm relies heavily on the initial calibration measurements. The proposed improvement here can also accommodate this issue and eliminate

the need for re-calibration after small modifications.

The memory consumption of the algorithm scales linearly with the number of total bits in the circuit. For our implementation, with four branches and 7-bit attenuators, the required memory is (8 bytes) $\times 2^{28}$ (4 bytes for constellation points, 4 bytes for corresponding input codes) plus the size of the index matrix, which is negligible compared to the LUT size. The memory consumption can be reduced while the cancellation performance is increased. Since the leak signal usually does not drastically change in a short time, it is possible to load only the necessary chunk of the LUT. Moreover, as seen from Fig. 4.1, the distribution of the points in the constellation is not uniform, and it exhibits a pattern. Instead of uniformly defining the amplitude and phase region boundaries, a tailored function can evenly distribute the number of samples in each region, increasing the algorithm performance.

The vector modulator topology used in this work is digitally controlled, and its noise contribution is acceptable compared to other noise sources. When the transmit noise is suppressed, and the receive noise becomes dominant, additive noise of the circuit will be one of the determining factors for the receive noise level.

However, in the case of STAR imaging, noise is not the only factor that affects image quality. Although the low-frequency variations, such as coupling variation due to load movement, can be observed and corrected at the expense of the scan time, fluctuations that happen during one TR (e.g., vibrations) are not possible to detect and correct with the current setup. For example, vibrations arising from the gradient switching affect the performance of the cancellation by modulating the coupling between the transmit and receive coils, and they result in artifacts in the final image. Using a volume coil as opposed to small loop coils grants stability, yet vibrations are observed on the residual signal envelope. In this work, the problem was circumvented by switching the gradients on 5 ms before the acquisition. More elegant solutions can be incorporated in the future to solve these issues, such as real-time tracking and compensation of the leak signal even during the reception via an independent receive chain.

A problem that needs to be addressed with this circuit is the transmit power loss due to the N-way power divisions with fixed phases. The power efficiency of the circuit can be improved by replacing the fixed phase shifters by digital step phase shifters. In this way, instead of destructively summing the power to synthesize the compensation signal, the same signal can be constructively synthesized by adjusting the phase. Besides, the importance of good passive decoupling is evident here, because, with better passive isolation, less power will be required to compensate for the leakage.

Another improvement in both the power efficiency and the cancellation performance could be made via optimizing the cancellation circuit for the coil. During the experiments, the phase and amplitude of the coupling do not change over time drastically. This behavior means that most of the samples in the constellation will never be used. Phase shifters can be adjusted so that only the necessary part of the complex plane is covered by the vector modulator. This optimization can be exploited to decrease the number of bits for reducing the complexity or increasing the cancellation performance.

Chapter 5

Vector Modulator Based Active Compensation of Direct Feedthrough in Magnetic Particle Imaging

5.1 Introduction

This work submitted as an abstract to International Workshop on Magnetic Particle Imaging (IWMPI) 2020 and awarded with a poster presentation.

In magnetic particle imaging (MPI), excitation and signal acquisition occurs simultaneously, leading to a direct feedthrough problem. The direct feedthrough is especially problematic considering the drastic disparity between the transmitted and received power. The direct feedthrough signal may saturate the pre-amplifier, reducing the dynamic range and the detection sensitivity. This in turn jeopardizes MPI's excellent promise of high sensitivity [54]. To tackle these issues, gradiometer receive coils are frequently used as a passive compensation method. However, these coils are difficult to design and tune perfectly, and the tuning is

prone to degradation due to external effects (e.g., vibration, heating). Even for a fine-tuned gradiometer coil, the remaining direct-feedthrough can still exceed the signal from a low concentration of magnetic nanoparticles (MNPs). To overcome challenges arising from passive compensation, active compensation methods have also been proposed in MPI [55, 56]. The elimination of direct-feedthrough is an active research area in other fields as well, such as telecommunications (full-duplex radio) [37, 38] and Magnetic Resonance Imaging (MRI) [31, 32, 17].

An active compensation method in MRI using a vector modulator structure based on copying the excitation signal and modifying it in analog domain [17] was proposed in Chapters 4 and 3. In this work, this technique was adapted to MPI for active compensation of the direct feedthrough. With experiments on an in-house Arbitrary Waveform Relaxometer (AWR), a significant increase in detection sensitivity was demonstrated at fundamental harmonic.

5.2 Material and Methods

For an amplitude modulated (AM) drive field (DF) with a center frequency of f_0 and envelope of $A(t)$, assuming coupling between drive and receive coil is time-invariant, the direct feedthrough signal can be formulated as,

$$s(t) = k \cdot A(t) \cdot \sin(2\pi f_0 t + \phi) \tag{5.1}$$

where k and ϕ are the attenuation coefficient and phase shift stemming from mutual coupling, respectively. Most active compensation methods estimate/measure parameters k and ϕ, and then reconstructs $s(t)$ given that the other parameters in Eq. (5.1) are known. In this work, instead of reconstructing direct-feedthrough, a low-amplitude copy of the transmit signal is taken directly from the input of the DF coil and modified in the analog domain, to match k and ϕ.

5.2.1 Active Compensation Circuit

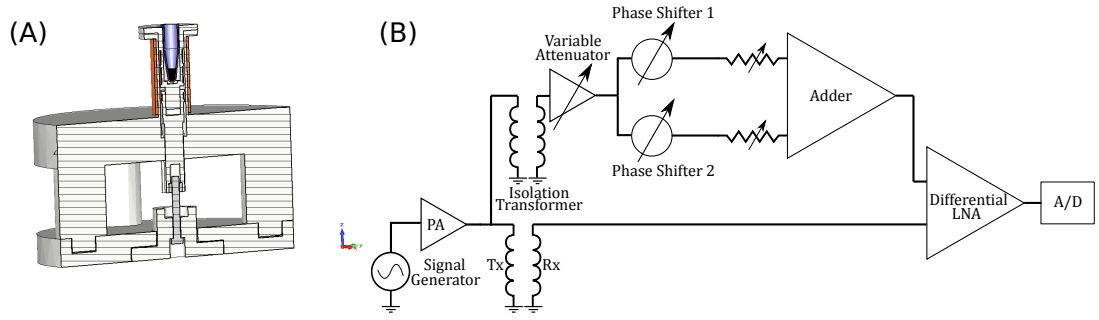

Figure 5.1: **(A)** Schematic of the in-house AWR. **(B)** Schematic of the system and compensation circuit, which acts as a vector modulator.

A circuit that can modify the phase and amplitude of its input was designed, as shown in Fig. 5.1. The circuit consisted of three stages. The first stage was a variable attenuator/amplifier that also acts as an input buffer. The next stage was divided into several branches containing phase shifters (unity gain all pass filters). The phase at f_0 can be adjusted by varying resistance R according to $\phi(2\pi f) = -2\tan^{-1}(2\pi f RC)$ for a low-pass topology and $\phi(2\pi f) = \pi - 2\tan^{-1}(2\pi f RC)$ for a high-pass topology. Hence, by combining multiple of these two phase shift elements, one can reach any desirable phase shift. The last stage acts as a combiner and consists of a summer Op-Amp. The weights of the summation operation can be adjusted with variable resistors in each branch. With weighted combination of these stages, (k, ϕ) parameter space can be covered efficiently.

The circuit can be built using $(n + 2)$ Op-Amps, where n is the number of desired branches. The number of branches is a trade-off between the degree of freedom, the coverage of parameter space and the circuit complexity. Here, TL082 Op-Amps were used to implement all stages.

In this work, a vector modulator is built where resistances for phase shifting and amplitude scaling are controlled manually via mechanical potentiometers. For AWR and MPI experiments, this circuit is used. A digitally controlled vector modulator is also designed and built. MCP4352 (Microchip Technology) is used as a digital potentiometer. Both of the implementations can be seen in Fig. 5.2.

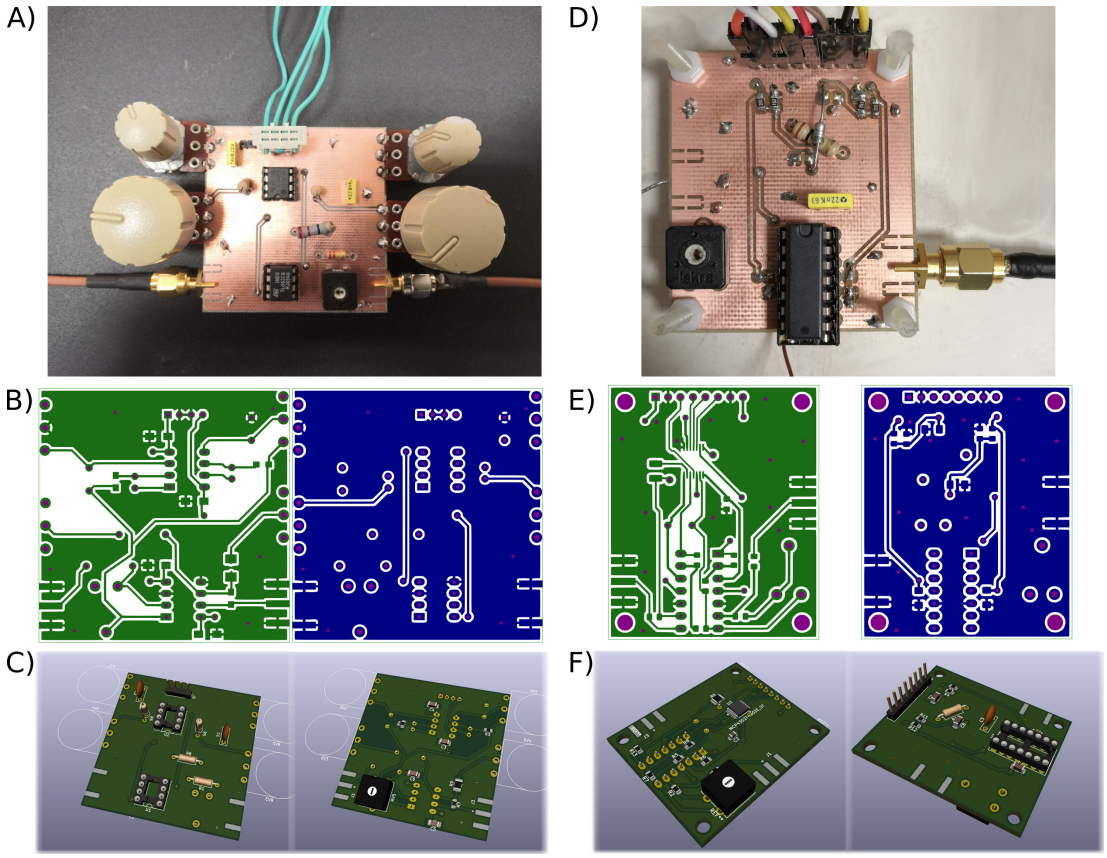

Figure 5.2: **(A)** The fabricated manually controlled vector modulator. **(B)** PCB layout of the manually controlled vector modulator. **(C)** 3D model of the manually controlled vector modulator. **(D)** The fabricated digitally controlled vector modulator. **(E)** PCB layout of the manually controlled vector modulator **(F)** 3D model of the manually controlled vector modulator.

The vector modulator together with the AWR setup is simulated in LTSpice software. Realistic component values, models and system measurements are incorporated in the simulation to verify the feasibility of the structure. Variable resistor values in the vector modulator are swept manually to minimize the compensated signal at 10.8 kHz. Variable resistors are utilized in the range between $100\,\Omega$ - $5\,k\Omega$ with a step size of $20\,\Omega$ as per the physical implementation.

5.2.2 Experiment Setup

The operation of the proposed technique was demonstrated on an in-house AWR, which had a DF coil with a small (3.1 µH) inductance that eliminated the need for impedance matching [57, 58]. The receiver coil was a gradiometer coil, with a manual adjustment knob to reach more than 80 dB decoupling. AM modulated waveforms were created by data acquisition card (DAQ) and amplified using a power amplifier (PA). The received signal was pre-amplified by a low noise amplifier (LNA) and digitized by the same DAQ. The compensation signal was copied from the output of the PA using an isolation transformer to isolate the DF and receive chains. The output of the circuit was subtracted from the received signal using the differential input of the LNA.

To demonstrate the increase in detection sensitivity, four samples of Perimag (Micromod GmbH, Germany) with dilution factors of ×2, ×8, ×40, and ×80 were prepared. Each sample had 20 µL total volume. DF at 5 mT and 10.8 kHz was applied. The first and the third harmonics were investigated with and without active compensation.

To show that the proposed structure does not distort the received signal or decrease the SNR, 1D MPI experiments are also performed with an in-house FFP MPI scanner [59]. 15 mT at 9.7 kHz sinusoidal drive field is applied. A phantom with two droplets of SPIOs is used for imaging. Scan time was around 30 minutes. Both line scans are reconstructed with standard x-space reconstruction [54] with a notch filter at the fundamental frequency and detrending correction.

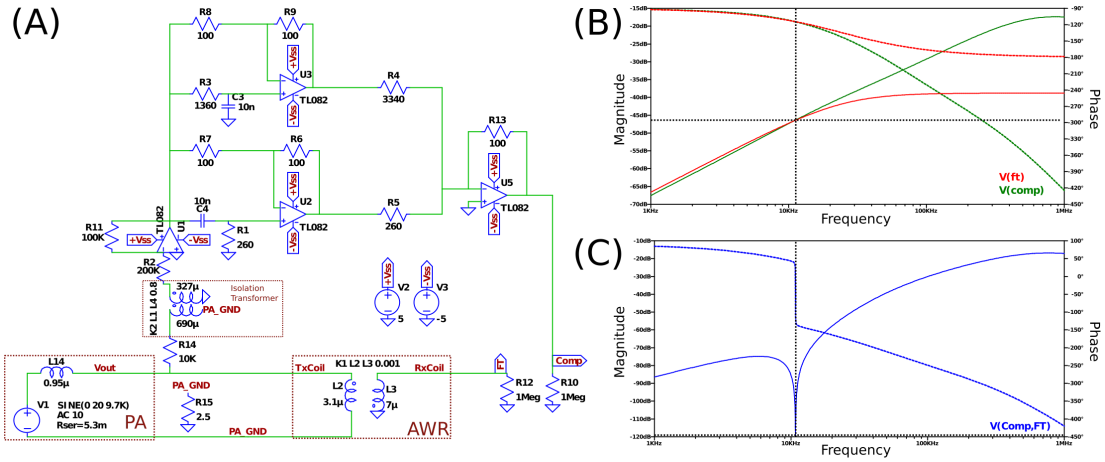

Figure 5.3: **(A)** Schematic of the LTSpice simulation of AWR setup and the vector modulator. **(B)** Frequency response of the schematic simulated between 1 kHz to 1MHz. $V(ft)$ is the direct-feedthrough voltage measured at the receive coil. $V(comp)$ is the compensation signal measured at the output of the vector modulator. The cursor marks the value at 10.8 kHz. **(C)** Frequency response of the compensated received signal. $V(Comp, FT)$ is the difference between feedthrough and the compensation signal $(V(ft) - V(comp))$. The cursor marks the value at 10.8 kHz.

5.3 Results

Simulation results can be seen in Fig. 5.3. At the target frequency (f_0 = 10.8 kHz), more than 70 dB additional isolation is achieved. During the optimization, it is observed that decent isolation can be obtained via different combinations of the resistor values, and it is possible to acquire larger isolation bandwidth by choosing a different combination. However, for this simulation, since minimization of the residual signal at a single frequency was chosen as the objective, bandwidth is quite narrow, and additional isolation drops to 10 dB at the second harmonic (21.6 kHz).

Despite the passive decoupling of the AWR, the remaining direct-feedthrough was still more than 40 dB above the noise level. With careful adjustment of the potentiometers in the active compensation circuit, the direct-feedthrough was successfully reduced to the noise floor, as shown in Fig. 5.4.

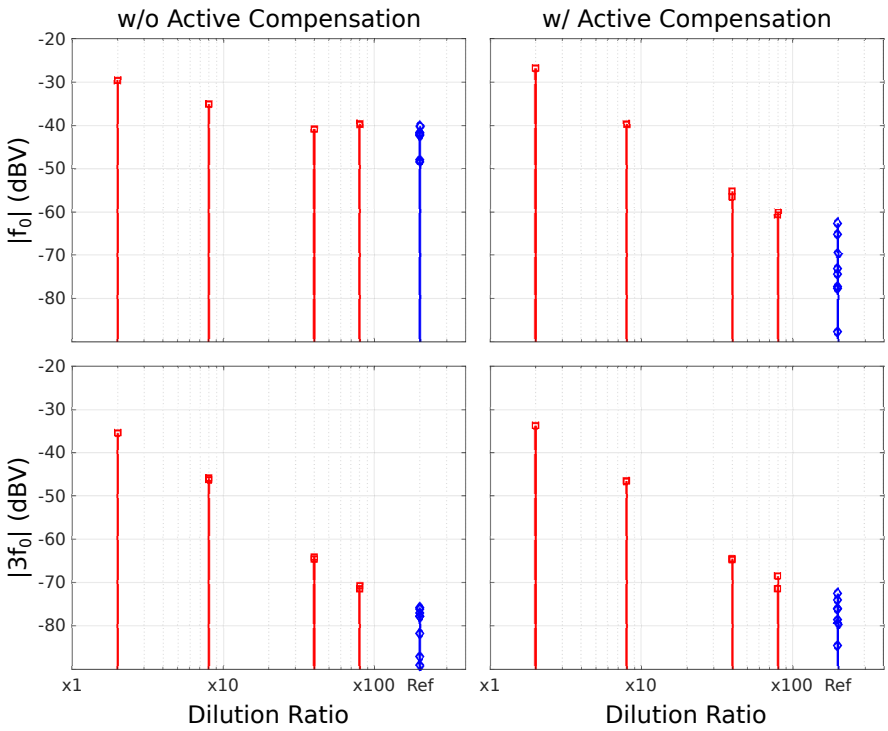

Figure 5.4: Signal at the fundamental harmonic and the third harmonic, with and without active compensation for four samples with different dilution factors. $f_0 = 10.8$ kHz.

Figure 5.4 shows a comparison at the fundamental and third harmonics, with and without active compensation. In both cases, signal amplitude at f_0 was above the direct-feedthrough for $\times 2$ and $\times 8$ dilutions. However, for $\times 40$ and $\times 80$ dilutions without active compensation, the MNP signal was dominated by the direct-feedthrough. For $\times 80$ dilution, since the third harmonic was reduced almost to noise level, it was not possible to detect the signal with the passive decoupling alone. In contrast, with active compensation, the MNP could be easily detected from the recovered fundamental harmonic, showing a significant improvement in sensitivity of up to 40 dB.

MPI experiment results can be seen in Fig. 5.5. The feedthrough level was reduced below the noise floor before the imaging experiment. During the experiment, an increase in the feedthrough level was observed. No distortion on the signal was observed after the compensation.

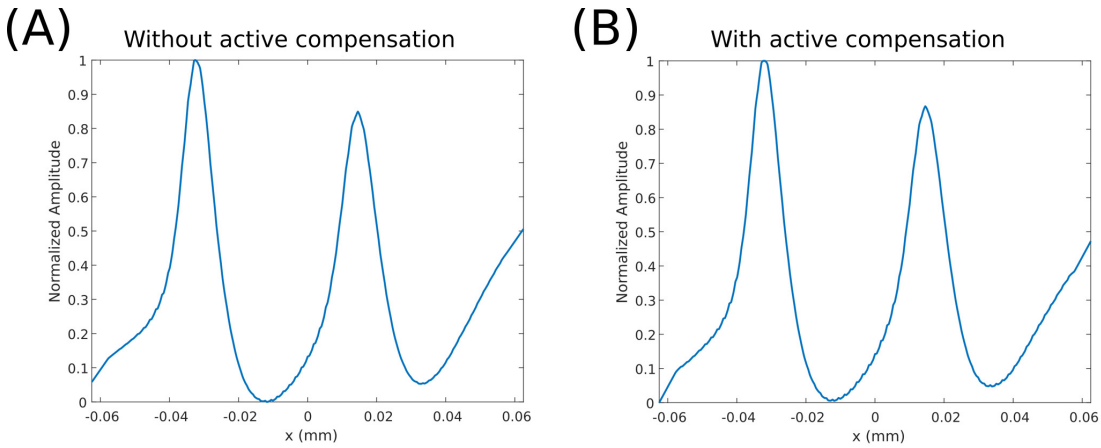

Figure 5.5: Line scan of a phantom without **(A)** and with **(B)** active compensation.

5.4 Discussion

There are two main advantages of this approach compared to the active compensation methods that use an independent signal source to create compensation signal [31, 56]. First, the addition of this circuit does not increase the noise floor, unlike other methods that add an independent noise source to the received signal. Next, our method is more robust against voltage drop of DF coil due to heating, since it will also be reflected on the compensation circuit input. However, a change in mutual coupling (e.g., due to vibrations etc.) will not be reflected. One potential solution could be to replace mechanical potentiometers with digital ones and automating the compensation process, which would also eliminate variations in compensation performance.

The direct feedthrough level could not be kept below the noise floor throughout the line scan experiment shown in 5.5. This is caused by two reasons, the first one is, both scans are reconstructed in the exact same ways, meaning fundamental frequencies are removed in both of the scans. Hence, it is expected that no improvement is seen due to a reduction in the feedthrough. The second reason is, active cancellation is only adjusted at the beginning of the scan, and no monitoring and correction is done throughout the scan. An increase in the feedthrough as the scan progressed was caused by the mechanical vibrations and the heating

of the coil. Using a shorter scan time might reduce the rise in the feedthrough; however, drift due to coil heating still could pose a problem. A better approach would be utilizing the digitally controlled vector modulator, as shown in Fig. 5.2 with an automated control algorithm. Our proposed algorithm in Chapter 4 is well-suited for this task. With these improvements, the feedthrough level can be kept below the noise floor, and it can be eliminated from the image. In this way, instead of filtering it out, the fundamental frequency can be utilized in the reconstruction, which would alleviate the need for DC correction and eliminate the artifact related to the DC shift.

As the single frequency excitation is used in these experiments, the bandwidth of the isolation is of no importance here. In fact, as can be seen in Fig. 5.3, compensation behaves like a notch filter at the target frequency. However, higher isolation bandwidth is desirable in the case that excitation is done with a multi-frequency signal. A second case where the bandwidth matters is the presence of the non-linearities in the system, usually originating from the transmit power amplifier. In this case, harmonics can also be contaminated with the feedthrough on top of the fundamental frequency. This was not the case in our AWR experiments since the passive decoupling of the gradiometer coil was high enough to suppress the harmonic interference below the noise floor. If isolation in a higher bandwidth is desired, optimization goal can be changed as minimizing the total residual signal power in the desired bandwidth, instead of minimizing the power at the fundamental frequency. During the manual optimization process, it is observed that bandwidth can be significantly increased at the cost of reduced maximum isolation by using different combinations of resistance values. In this way, an additional 40 dB isolation within the bandwidth of 50 kHz was possible. In most cases, 40 dB of further isolation is enough to suppress the feedthrough below the noise floor.

Chapter 6

Conclusion

In Chapter 4, a look-up table based control algorithm for digitally controlled vector modulators is proposed. The algorithm enables STAR imaging since it allows us to dynamically isolate transmit and receive channels. The performance of the algorithm along with a vector modulator structure is demonstrated in this chapter. With the proposed algorithm and the hardware, in combination with the passive cancellation, more than 80 dB of isolation can be achieved. Continuous SWIFT images acquired with the proposed method is shown and evaluated. Due to low bandwidth of the isolation, images are acquired with less than 7 kHz of bandwidth, which resulted in susceptibility artifact. However, since we achieved sufficient isolation (>80 dB) in this band, there were no need for applying digital subtraction at the post-processing.

It can be claimed that the algorithm can enable real-time cancellation of time-varying leak signals coming from the transmit chain. Convergence time of the algorithm requires investigation; however, initial observations suggest that less than 10 iterations, which takes around 50 ms was sufficient to achieve -80 dB threshold. The algorithm offers the flexibility of further improvement, and it can be used for many different types of digitally controlled cancellation circuits. In the future, the proposed design can circumvent the issues causing the time-varying leak signal, such as load variation, temperature changes, etc., which will

also allow STAR imaging of the moving tissues, such as chest and abdomen.

In Chapter 3, noise in STAR imaging is analyzed, and the trade-offs between the parameters of the STAR system and the transmit chain are laid-out as a guideline for future applications of STAR in MRI. Furthermore, it is shown that the transmit noise can be isolated with cancellation in the analog domain. It is claimed that usage of the conventional transmit chains with high gain (>60 dB) and high noise is possible for STAR imaging, which can enable higher flip angles and alleviates the need for replacing the transmit amplifier. It is shown that there is sufficient isolation needed for achieving thermal noise at the receive side. After this sufficient isolation is attained, removing the residual signal in post-processing does not impose SNR loss. With the possibility of using conventional amplifiers, STAR imaging can be possible with less scanner modification. The isolation threshold for the STAR system can be selected according to transmit system parameters and imaging bandwidth. This analysis is verified with a low-noise vector modulator structure in combination with the previously proposed algorithm.

In Chapter 5, a vector modulator active compensation circuit is proposed for the direct feedthrough problem in MPI. This method copies the excitation signal and modifies in analog domain, reducing the direct feedthrough signal down to noise floor. This method achieves a significant increase in detection sensitivity at fundamental harmonic. It is claimed that, by combining the digital implementation of the vector modulator and the proposed algorithm in Chapter 4, dynamic cancellation of the feedthrough can be achieved and fundamental harmonic can be completely recovered to be used in image reconstruction, particle parameter estimation or particle detection. In the experiments, around 30 dB of isolation was enough to reduce the feedthrough down to the noise level. In the simulations, it was shown that more than 50 dB of active isolation is possible with this setup. By recovering the fundamental frequency, detection sensitivity is increased by more than 10 dB. With the adaption of automated cancellation, fundamental frequency can also be recovered and utilized in the imaging, which will increase the SNR and reduce the DC shift related artifacts in MPI.

Bibliography

[1] Y. Okada, T. Kawai, and A. Enokihara, "Compact lumped-element 5-way wilkinson power divider with broadband operation," in *2016 46th European Microwave Conference (EuMC)*, (London, UK), pp. 202–205, IEEE, Oct. 2016.

[2] B. Gleich and J. Weizenecker, "Tomographic imaging using the nonlinear response of magnetic particles," *Nature*, vol. 435, pp. 1214–1217, June 2005. Number: 7046 Publisher: Nature Publishing Group.

[3] P. W. Goodwill, E. U. Saritas, L. R. Croft, T. N. Kim, K. M. Krishnan, D. V. Schaffer, and S. M. Conolly, "X-Space MPI: Magnetic Nanoparticles for Safe Medical Imaging," *Advanced Materials*, vol. 24, no. 28, pp. 3870–3877, 2012. _eprint: https://www.onlinelibrary.wiley.com/doi/pdf/10.1002/adma.201200221.

[4] E. U. Saritas, P. W. Goodwill, L. R. Croft, J. J. Konkle, K. Lu, B. Zheng, and S. M. Conolly, "Magnetic Particle Imaging (MPI) for NMR and MRI Researchers," *J Magn Reson*, vol. 229, pp. 116–126, Apr. 2013.

[5] J. Rahmer, D. Wirtz, C. Bontus, J. Borgert, and B. Gleich, "Interactive Magnetic Catheter Steering With 3-D Real-Time Feedback Using Multi-Color Magnetic Particle Imaging," *IEEE Trans Med Imaging*, vol. 36, no. 7, pp. 1449–1456, 2017.

[6] B. Zheng, M. P. von See, E. Yu, B. Gunel, K. Lu, T. Vazin, D. V. Schaffer, P. W. Goodwill, and S. M. Conolly, "Quantitative Magnetic Particle Imaging

Monitors the Transplantation, Biodistribution, and Clearance of Stem Cells In Vivo," *Theranostics*, vol. 6, pp. 291–301, Jan. 2016.

[7] C. Stehning, B. Gleich, and J. Rahmer, "Simultaneous magnetic particle imaging (MPI) and temperature mapping using multi-color MPI," *International Journal on Magnetic Particle Imaging*, vol. 2, Dec. 2016. Number: 2.

[8] M. Utkur, Y. Muslu, and E. U. Saritas, "Relaxation-based viscosity mapping for magnetic particle imaging," *Phys. Med. Biol.*, vol. 62, pp. 3422–3439, Apr. 2017. Publisher: IOP Publishing.

[9] Y. Muslu, M. Utkur, O. B. Demirel, and E. U. Saritas, "Calibration-Free Relaxation-Based Multi-Color Magnetic Particle Imaging," *IEEE Transactions on Medical Imaging*, vol. 37, pp. 1920–1931, Aug. 2018. Conference Name: IEEE Transactions on Medical Imaging.

[10] E. E. Mason, C. Z. Cooley, S. F. Cauley, M. A. Griswold, S. M. Conolly, and L. L. Wald, "Design analysis of an MPI human functional brain scanner," *Int J Magn Part Imaging*, vol. 3, no. 1, 2017.

[11] D. Nishimura, *Principles of magnetic resonance imaging*. Stanford University, 1996.

[12] D. Idiyatullin, S. Suddarth, C. A. Corum, G. Adriany, and M. Garwood, "Continuous SWIFT," *Journal of Magnetic Resonance*, vol. 220, pp. 26–31, July 2012.

[13] M. Weiger, K. P. Pruessmann, M. Tabbert, and F. Hennel, "Sampling Strategies for MRI with Simultaneous Excitation and Acquisition," in *Proc. Intl. Soc. Mag. Reson. Med. 17*, p. 1, 2009.

[14] M. A. Bernstein, K. F. King, and Z. J. Zhou, *Handbook of MRI pulse sequences*. Amsterdam ; Boston: Academic Press, 2004.

[15] J. Jackson, C. Meyer, D. Nishimura, and A. Macovski, "Selection of a convolution function for Fourier inversion using gridding (computerised tomography application)," *IEEE Transactions on Medical Imaging*, vol. 10, pp. 473–478, Sept. 1991. Conference Name: IEEE Transactions on Medical Imaging.

[16] B. Hargreaves and Beatty, Philip, "Gridding Functions," 2004.

[17] B. Tasdelen, A. Sadeghi-Tarakameh, U. Yilmaz, and E. Atalar, "Dynamic Decoupling for Simultaneous Transmission and Acquisition in MRI," in *Proc. Intl. Soc. Mag. Reson. Med. 27*, (Montreal), May 2019.

[18] F. Bloch, W. W. Hansen, and M. Packard, "The Nuclear Induction Experiment," *Phys. Rev.*, vol. 70, pp. 474–485, Oct. 1946.

[19] W. A. Anderson, "Applications of Modulation Techniques to High Resolution Nuclear Magnetic Resonance Spectrometers," *Review of Scientific Instruments*, vol. 33, pp. 1160–1166, Nov. 1962.

[20] M. D. Robson, P. D. Gatehouse, M. Bydder, and G. M. Bydder, "Magnetic Resonance: An Introduction to Ultrashort TE (UTE) Imaging," *Journal of Computer Assisted Tomography*, vol. 27, pp. 825–846, Dec. 2003.

[21] C. J. Bergin, J. M. Pauly, and A. Macovski, "Lung parenchyma: projection reconstruction MR imaging.," *Radiology*, June 1991.

[22] C. J. Bergin, D. C. Noll, J. M. Pauly, G. H. Glover, and A. Macovski, "MR imaging of lung parenchyma: a solution to susceptibility.," *Radiology*, vol. 183, pp. 673–676, June 1992.

[23] S. Hafner, "Fast imaging in liquids and solids with the Back-projection Low Angle ShoT (BLAST) technique," *Magnetic Resonance Imaging*, vol. 12, pp. 1047–1051, Jan. 1994.

[24] Y. Wu, J. L. Ackerman, D. A. Chesler, J. Li, R. M. Neer, J. Wang, and M. J. Glimcher, "Evaluation of Bone Mineral Density Using Three-Dimensional Solid State Phosphorus-31 NMR Projection Imaging," *Calcif Tissue Int*, vol. 62, pp. 512–518, June 1998.

[25] D. P. Madio and I. J. Lowe, "Ultra-fast imaging using low flip angles and fids," *Magnetic Resonance in Medicine*, vol. 34, no. 4, pp. 525–529, 1995.

[26] D. O. Kuethe, A. Caprihan, E. Fukushima, and R. A. Waggoner, "Imaging lungs using inert fluorinated gases," *Magnetic Resonance in Medicine*, vol. 39, no. 1, pp. 85–88, 1998.

[27] M. Weiger, K. P. Pruessmann, and F. Hennel, "MRI with zero echo time: Hard versus sweep pulse excitation," *Magnetic Resonance in Medicine*, vol. 66, no. 2, pp. 379–389, 2011.

[28] D. Idiyatullin, C. Corum, J.-Y. Park, and M. Garwood, "Fast and quiet MRI using a swept radiofrequency," *Journal of Magnetic Resonance*, vol. 181, pp. 342–349, Aug. 2006.

[29] D. Idiyatullin, C. Corum, S. Moeller, and M. Garwood, "Gapped Pulses for Frequency-Swept MRI," *J Magn Reson*, vol. 193, pp. 267–273, Aug. 2008.

[30] S.-M. Sohn, J. T. Vaughan, R. L. Lagore, M. Garwood, and D. Idiyatullin, "In vivo MR imaging with simultaneous RF transmission and reception," *Magn Reson Med*, vol. 76, no. 6, pp. 1932–1938, 2016.

[31] A. C. Özen, M. Bock, and E. Atalar, "Active decoupling of RF coils using a transmit array system," *Magnetic Resonance Materials in Physics, Biology and Medicine*, vol. 28, pp. 565–576, Dec. 2015.

[32] A. C. Özen, E. Atalar, J. G. Korvink, and M. Bock, "In vivo MRI with Concurrent Excitation and Acquisition using Automated Active Analog Cancellation," *Scientific Reports*, vol. 8, Dec. 2018.

[33] M. Salim, A. C. Ozen, M. Bock, and E. Atalar, "Active Decoupling of Transmit and Receive Coils for Full-Duplex MRI," *arXiv:1810.10973 [physics]*, Oct. 2018. arXiv: 1810.10973.

[34] R. F. Lee, R. O. Giaquinto, and C. J. Hardy, "Coupling and decoupling theory and its application to the MRI phased array," *Magnetic Resonance in Medicine*, vol. 48, no. 1, pp. 203–213, 2002.

[35] Z. Mahmood, B. Guérin, E. Adalsteinsson, L. L. Wald, and L. Daniel, "An Automated Framework to Decouple pTx Arrays with Many Channels," in *Proc. Intl. Soc. Mag. Reson. Med. 21*, (Utah, USA), p. 1, 2013.

[36] Z. Mahmood, P. McDaniel, B. Guérin, B. Keil, M. Vester, E. Adalsteinsson, L. L. Wald, and L. Daniel, "General design approach and practical realization of decoupling matrices for parallel transmission coils," *Magnetic Resonance in Medicine*, vol. 76, pp. 329–339, July 2016.

[37] D. Bharadia, E. McMilin, and S. Katti, "Full duplex radios," in *ACM SIGCOMM Computer Communication Review*, vol. 43, (Hong Kong, China), pp. 375–386, ACM, 2013.

[38] C. B. Barneto, T. Riihonen, M. Turunen, L. Anttila, M. Fleischer, K. Stadius, J. Ryynänen, and M. Valkama, "Full-Duplex OFDM Radar With LTE and 5G NR Waveforms: Challenges, Solutions, and Measurements," *IEEE Transactions on Microwave Theory and Techniques*, pp. 1–13, 2019.

[39] M. Salim and E. Atalar, *Full-duplex MRI for zero TE imaging*. The Department of Electrical and Electronic Engineering, 2016.

[40] Y.-C. JEONG, "DESIGN OF A NOVEL VECTOR MODULATOR," *Microwave Journal*, vol. 44, p. 156, Oct. 2001. Section: 156.

[41] X. Yan, Z. Cao, and W. A. Grissom, "Ratio-adjustable power splitters for array-compressed parallel transmission," *Magnetic Resonance in Medicine*, vol. 79, pp. 2422–2431, Apr. 2018.

[42] D.-J. van den Broek, E. A. M. Klumperink, and B. Nauta, "An In-Band Full-Duplex Radio Receiver With a Passive Vector Modulator Downmixer for Self-Interference Cancellation," *IEEE Journal of Solid-State Circuits*, vol. 50, pp. 3003–3014, Dec. 2015. Conference Name: IEEE Journal of Solid-State Circuits.

[43] Y. Okada, T. Kawai, and A. Enokihara, "Design method of unequal Wilkinson power divider using LC-ladder circuits for multi-way power dividers," in *2016 Asia-Pacific Microwave Conference (APMC)*, (New Delhi, India), pp. 1–4, IEEE, Dec. 2016.

[44] C. A. Corum, D. S. Idiyatullin, S. Moeller, and M. G. Garwood, "Multistep correction for angle consistent artifacts in radial sampled datasets," Apr. 2013.

[45] K. T. Block and M. Uecker, "Simple Method for Adaptive Gradient-Delay Compensation in Radial MRI," in *Proc. Intl. Proc. Intl. Soc. Mag. Reson. Med. 19*, p. 1, 2011.

[46] H. Schomberg, "Off-resonance correction of MR images," *IEEE Transactions on Medical Imaging*, vol. 18, pp. 481–495, June 1999.

[47] B. Tasdelen, A. Sadeghi-Tarakameh, U. Yilmaz, and E. Atalar, "Noise Analysis for Simultaneous Transmission and Reception Enabled MRI Scanner," in *Proc. Intl. Soc. Mag. Reson. Med. 28*, Aug. 2020.

[48] M. Garwood, D. Idiyatullin, C. A. Corum, R. Chamberlain, S. Moeller, N. Kobayashi, L. J. Lehto, J. Zhang, R. O'Connell, M. Tesch, M. J. Nissi, J. Ellermann, and D. R. Nixdorf, "Capturing Signals from Fast-relaxing Spins with Frequency-Swept MRI: SWIFT," in *eMagRes*, American Cancer Society, 2012.

[49] C. D. Motchenbacher and J. A. Connelly, *Low-noise electronic system design*. New York: Wiley, 1993.

[50] J. Phillips and K. Kundert, "Noise in mixers, oscillators, samplers, and logic an introduction to cyclostationary noise," in *Proceedings of the IEEE 2000 Custom Integrated Circuits Conference (Cat. No.00CH37044)*, (Orlando, FL, USA), pp. 431–438, IEEE, 2000.

[51] K. A. Kouznetsov and R. G. Meyer, "Phase Noise in LC Oscillators," *IEEE Journal of Solid-State Circuits*, vol. 35, no. 8, p. 5, 2000.

[52] T. Lee and A. Hajimiri, "Oscillator phase noise: a tutorial," *IEEE Journal of Solid-State Circuits*, vol. 35, pp. 326–336, Mar. 2000. Conference Name: IEEE Journal of Solid-State Circuits.

[53] M. Flanagan and G. Zimmerman, "Spur-reduced digital sinusoid synthesis," *IEEE Trans. Commun.*, vol. 43, pp. 2254–2262, July 1995.

[54] P. W. Goodwill and S. M. Conolly, "The X-Space Formulation of the Magnetic Particle Imaging Process: 1-D Signal, Resolution, Bandwidth, SNR, SAR, and Magnetostimulation," *IEEE Transactions on Medical Imaging*, vol. 29, pp. 1851–1859, Nov. 2010.

[55] B. Zheng, W. Yang, T. Massey, P. W. Goodwill, and S. M. Conolly, "High-power active interference suppression in magnetic particle imaging," in *2013 International Workshop on Magnetic Particle Imaging (IWMPI)*, pp. 1–1, Mar. 2013.

[56] D. Pantke, N. Holle, A. Mogarkar, M. Straub, and V. Schulz, "Multifrequency magnetic particle imaging enabled by a combined passive and active drive field feed-through compensation approach," *Medical Physics*, vol. 46, no. 9, pp. 4077–4086, 2019.

[57] C. B. Top, "An arbitrary waveform magnetic nanoparticle relaxometer with an asymmetrical three-section gradiometric receive coil," *Turk J Elec Eng & Comp Sci*, vol. In Press, 2019.

[58] Z. W. Tay, P. W. Goodwill, D. W. Hensley, L. A. Taylor, B. Zheng, and S. M. Conolly, "A High-Throughput, Arbitrary-Waveform, MPI Spectrometer and Relaxometer for Comprehensive Magnetic Particle Optimization and Characterization," *Sci Rep*, vol. 6, pp. 1–12, Sept. 2016.

[59] M. Utkur, Y. Muslu, and E. U. Saritas, "A 4.8 T/m magnetic particle imaging scanner design and construction," in *Proc. 21st National Biomedical Engineering Meeting*, Nov. 2017.

Appendix A

Calculation of the Component Values

A.1 Phase Shifters

In this section, necessary equations for calculating the component values for 90° (implemented with a high-pass tee) and 270° (implemented with a high-pass pi) phase shifters are given. 180° phase shifter is omitted since it is implemented as two 90° phase shifters in series.

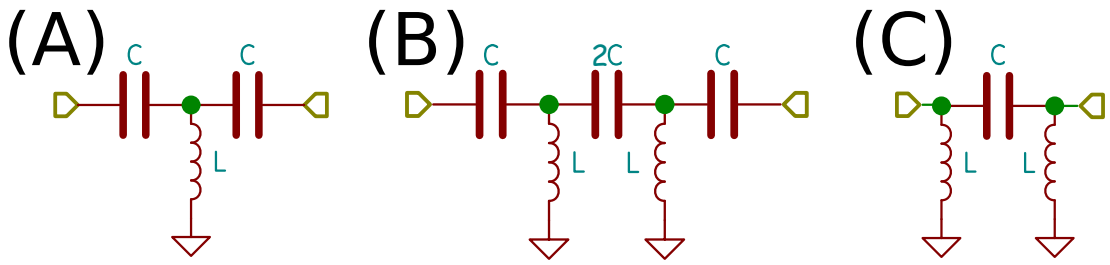

Figure A.1: **(A)** High-pass tee phase shifter. **(B)** Two high-pass tee phase shifter in series for doubling phase shift. **(C)** High-pass pi phase shifter.

For a high-pass tee phase shifter:

$$C = \frac{\sin(\phi)}{2 \cdot \pi \cdot f \cdot Z_0 \cdot (1 - \cos(\phi))} \tag{A.1}$$

$$L = \frac{Z_0}{2 \cdot \pi \cdot f \cdot \sin(\phi)} \tag{A.2}$$

For a high-pass pi phase shifter:

$$C = \frac{1}{2 \cdot \pi \cdot f \cdot Z_0 \cdot \sin(\phi)} \tag{A.3}$$

$$L = \frac{Z_0 \cdot \sin(\phi)}{2 \cdot \pi \cdot f \cdot (1 - \cos(\phi))} \tag{A.4}$$

Both phase shifter structures can be replaced with the low-pass versions as desired. The choice of a high-pass or a low-pass phase shifter can be made according to the frequency and phase response of the rest of the network. Since the exact phase values of the phase shifters are not critical, they can be tuned to acquire a flatter response, or to match the response of the circuit to the response of the coil coupling.

A.2 Wilkinson Divider

Schematic of the divider and even-odd mode analysis of the circuit is given in Fig. A.2. In this section, equations necessary to calculate component values are driven by using the even-odd mode analysis as suggested in Okada et al.[43].

For a division ratio K such that $K^2 = \frac{|S_{31}|^2}{|S_{21}|^2}$, characteristic impedance Z_0 and center frequency ω, the even-mode odd-mode analysis equations can be derived. Port resistances are as following:

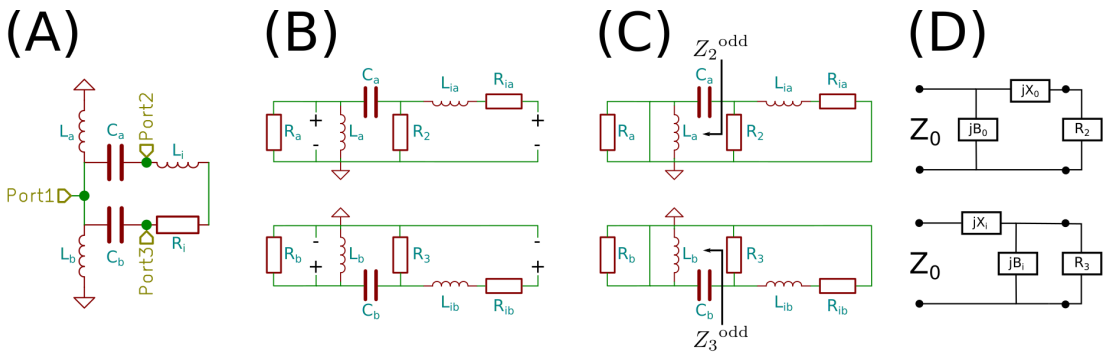

Figure A.2: **(A)** Schematic of the Wilkinson Power divider. If an unequal division ratio is desired, additional matching circuitry is required after the Port 2 and Port 3. **(B)** Even-mode analysis of the circuit. **(C)** Odd-mode analysis of the circuit. **(D)** Matching circuits for the Port 2 (top) which satisfies $R_2 < Z_0$ and for the Port 3 (bottom) which satisfies $R_3 > Z_0$ by convention.

$$R_2 = Z_0 \cdot K \tag{A.5}$$

$$R_3 = \frac{Z_0}{K} \tag{A.6}$$

$$R_a = (1 + K^2) \cdot Z_0 \tag{A.7}$$

$$R_b = (1 + 1/K^2) \cdot Z_0 \tag{A.8}$$

For the upper half circuit in Fig. A.2-B:

$$R_a = \left(\frac{1}{j\omega C_a} + R_2\right) //(j\omega L_a) \tag{A.9}$$

$$R_a = \frac{1}{\frac{1}{j\omega L_a} + \frac{j\omega C_a}{1+j\omega C_a R_2}} = \frac{j\omega L_a - \omega^2 L_a C_a R_2}{1 + j\omega C_a R_2 - \omega^2 L_a C_a} \tag{A.10}$$

$$j\omega L_a - \omega^2 L_a C_a R_2 = R_a + j\omega C_a R_2 R_a - \omega^2 L_a C_a R_a \tag{A.11}$$

Equating real and imaginary parts separately:

$$L_a = C_a R_2 R_a \tag{A.12}$$

$$R_a = \omega^2 L_a C_a (R_a - R_2) \tag{A.13}$$

Using the two equations above:

$$C_a = \sqrt{\frac{1}{\omega^2 R_2 (R_a - R_2)}} \tag{A.14}$$

$$L_a = \sqrt{\frac{R_a^2 R_2}{\omega^2 (R_a - R_2)}} \tag{A.15}$$

For the even-mode lower half circuit in Fig. A.2-B:

$$R_b = \left(\frac{1}{j\omega C_b} + R_3 \right) //(j\omega L_b) \tag{A.16}$$

$$C_b = \sqrt{\frac{1}{\omega^2 R_3 (R_b - R_3)}} \tag{A.17}$$

$$L_b = \sqrt{\frac{R_b^2 R_3}{\omega^2 (R_b - R_3)}} \tag{A.18}$$

For the odd-mode analysis that can be seen in the Fig. A.2-C upper half circuit:

$$Z_2^{\text{odd}} = \frac{R_2}{1 + j\omega C_a R_2} = \frac{R_2 - j\omega C_a R_2^2}{1 + \omega^2 C_a^2 R_2^2} \tag{A.19}$$

$$\mathrm{Re}\{Z_2^{\mathrm{odd}}\} = R_{ia} = \frac{R_2}{1+\omega^2 C_a^2 R_2^2} \tag{A.20}$$

$$\mathrm{Im}\{Z_2^{\mathrm{odd}}\} = -\omega L_{ia} = -\frac{\omega C_a R_2^2}{1+\omega^2 C_a^2 R_2^2} \tag{A.21}$$

$$L_{ia} = -\frac{C_a R_2^2}{1+\omega^2 C_a^2 R_2^2} \tag{A.22}$$

Equations of the lower half circuit for the odd-mode analysis (Fig. A.2-C):

$$\mathrm{Re}\{Z_3^{\mathrm{odd}}\} = R_{ib} = \frac{R_3}{1+\omega^2 C_b^2 R_3^2} \tag{A.23}$$

$$\mathrm{Im}\{Z_3^{\mathrm{odd}}\} = -\omega L_{ib} = -\frac{\omega C_b a R_3^2}{1+\omega^2 C_b^2 R_3^2} \tag{A.24}$$

$$L_{ib} = -\frac{C_b R_3^2}{1+\omega^2 C_b^2 R_3^2} \tag{A.25}$$

For the final circuit in Fig. A.2-A, $L_i = L_{ia} + L_{ib}$ and $R_i = R_{ia} + R_{ib}$. Note that, if the division ratio is equal ($K = 1$), $L_{ia} = L_{ib}$, $R_{ia} = R_{ib}$, $C_a = C_b$ and $R_2 = R_3$. Then the equations for L_i and R_i can be simplified as:

$$L_i = -\frac{2C_a R_2^2}{1+\omega^2 C_a^2 R_2^2} \tag{A.26}$$

$$R_i = \frac{2R_2}{1+\omega^2 C_a^2 R_2^2} \tag{A.27}$$

For the equal divider, there is no need for a matching circuit since the ports are already matched to Z_0. For the unequal divider, a matching circuit as given

in the schematic at Fig. A.2-D for the Port 2 ($R_2 < Z_0$) can be implemented as following:

$$X_0 = -\sqrt{\frac{-(2R_2^3 - Z_0R_2^2) + \sqrt{(2R_2^3 - Z_0R_2^2)^2 - 4R_2(Z_0R_2^4 + R_2^5)}}{2R_2}} \tag{A.28}$$

$$B_0 = -\left(X_0 + \frac{R_2^2}{X_0}\right) \tag{A.29}$$

$$C_0 = -\frac{1}{X_0\omega} \tag{A.30}$$

$$L_0 = -\frac{B_0}{\omega} \tag{A.31}$$

where L_0 is the inductor value for acquiring the impedance B_0, and C_0 is the capacitance value for acquiring the impedance X_0. For the Port 3 ($R_3 > Z_0$):

$$B_i = R_3\sqrt{\frac{Z_0}{R_3 - 1}} \tag{A.32}$$

$$X_i = -\frac{B_iR_3^2}{R_3^2 + B_i^2} \tag{A.33}$$

$$C_i = -\frac{1}{X_i\omega} \tag{A.34}$$

$$L_i = \frac{B_i}{\omega} \tag{A.35}$$

where L_i is the inductor value for acquiring the impedance B_i, and C_i is the capacitance value for acquiring the impedance X_i.